Natural Resources Canada | Ressources naturelles Canada

GEOLOGICAL SURVEY OF CANADA
OPEN FILE 8995

Near real-time processing of NRCan riometer data

R.A.D. Fiori, K. Reiter, D. Galeschuk, T. Ghosal, and N. Olfert

2023

Canada

GEOLOGICAL SURVEY OF CANADA
OPEN 8995

Near real-time processing of NRCan riometer data

R.A.D. Fiori, K. Reiter, D. Galeschuk, T. Ghosal, and N. Olfert

2023

Permanent link: https://doi.org/10.4095/332078

This publication is available for free download through GEOSCAN (https://geoscan.nrcan.gc.ca/).

Recommended citation
Fiori, R.A.D., Reiter, K., Galeschuk, D., Ghosal, T., and Olfert, N., 2023. Near real-time processing of NRCan riometer data; Geological Survey of Canada, Open File 8995, 30 p. https://doi.org/10.4095/332078

Publications in this series have not been edited; they are released as submitted by the author.

ISSN 2816-7155
ISBN 978-0-660-49943-7
Catalogue No. M183-2/8995E-PDF

Table of Contents

1. Introduction

High frequency (HF; 3-30 MHz) radio wave propagation is sensitive to ionospheric absorption that leads to a reduction in the overall signal strength and controls the lower boundary of the useable frequency range (e.g. Browne et al., 1995). Absorption is caused by the interaction of radio waves with ionospheric particles. Radio wave energy is transferred to charged ionospheric particles and then lost through collisions of those charged particles with neutral particles before being reradiated. Absorption is typically considered to be a D-region (~70-90 km altitude) phenomenon due to the high density of neutral particles at D-region altitudes which increases the particle collision rate causing the radio waves to be dispersed, or absorbed as heat, reducing the signal strength. Absorption is an important consideration for technologies with HF dependencies. Examples include HF communications relied on by aviation, maritime users, military, and emergency response, (e.g., Agy, 1970; Cannon et al., 2013; Coyne, 1979; Knipp et al., 2021; National Research Council, 2008; Neal et al., 2013; Pirjola et al., 2005), over-the-horizon radar (OTHR) used for long-range surveillance (Thayaparan et al., 2018), and research (e.g. Chisham et al., 2007).

D-region absorption is also highly dependent on the ionospheric vertical electron density profile. The ionosphere itself is formed through both photoionization reactions between solar photons and neutral particles in the Earth's ionosphere, and collisions between energetic particle precipitation and these same neutral particles (e.g., Browne et al., 1995; Hunsucker and Hargreaves, 2003). The ionospheric production process is controlled by solar-magnetosphere-ionosphere-atmosphere coupling processes which drive predictable changes in the ionospheric electron density. Absorption due to these processes can be calculated using the Appleton-Hartree equation (Davies, 1990) in combination with various ionospheric electron density, magnetic field, and collision frequency models (Zawdie et al., 2017). Absorption models built from climatological electron density, magnetic field, and collision frequency models do not, however, include contributions from ionospheric disturbances driven by space weather.

There are three primary types of space weather driven absorption: shortwave fadeout, auroral absorption, and polar cap absorption. Shortwave fadeout is absorption due to enhanced photoionization on the dayside of the Earth due to a solar X-ray flare (Mitra, 1974). Shortwave fadeout lasts on the order of 10-s of minutes to hours, and is most strongly felt near the subsolar point, which is the point on the Earth where the sun is directly overhead, falling off toward the terminator (Davies, 1990). Auroral absorption is driven by the precipitation of energetic (>30 kV) electrons at auroral latitudes, usually during a period of enhanced geomagnetic activity (e.g., Baker et al., 1981; Hargreaves, 1969; Newell et al., 2001; Fiori et al., 2020). Polar cap absorption is caused by the precipitation of solar energetic protons into the high-latitude ionosphere typically in conjunction with a solar flare or coronal mass ejection (e.g., Kavanagh et al., 2004a; Neal et al., 2013). For information on the typical duration and occurrence frequency of these three types of absorption, see Fiori et al. (2022b).

Development of operational space weather services that characterize the impact of space weather on HF radio wave propagation requires information on the characteristics and expected duration of space weather phenomena. Absorption due to space weather can be modelled using physics-based models (e.g., Levine et al., 2019), or empirical models (e.g., Sauer and Wilkinson, 2008; Foppiano and Bradley, 1983), which can be optimized through the inclusion of absorption data (e.g., Rogers and Honary, 2015; Fiori et al., 2022a). Absorption is derived from a relative ionospheric opacity meter, or riometer, described in Section 2. Operational services require this data be available in near-real time. Due to the method by

which absorption is derived from a riometer, and the potential for a noisy data set, this is not a simple task.

The objective of this work is to develop near-real time riometer data processing techniques, including data filtering and quiet day curve fitting to improve the accuracy of real-time riometer data. This report describes the algorithm NRCan has developed for processing riometer data in near-real time. In Section 2, riometer instruments used in the NRCan riometer array are described. The basic algorithm for near-real time processing of riometer data for operational use is described in Section 3. Section 4 explains how to identify periods where shortwave fadeout, auroral absorption, and polar cap absorption are expected to be observed in riometer data based on observed conditions. Identification of these periods is vital for modeling the quiet-day riometer response necessary for calculating absorption. Section 5 describes techniques for downsampling riometer data to calculate the quiet day curve, which is described and evaluated in Section 6. The methodologies described in this report form a robust data processing algorithm for handling real-time riometer data for operational use.

2. Riometer: Instrumentation and data collection

Riometer instruments are stationary passive radio antennas that measure the intensity of background cosmic radio noise from extraterrestrial sources (e.g. star, planet, galaxy) to characterize ionospheric opacity (Browne et al., 1995; Little and Leinback, 1959). Radio waves from these sources are partially absorbed in the D-region ionosphere, resulting in temporal variation of the received signal that can be amplified by ionospheric disturbances.

The sun, the Earth's closest star, is also a continuous source of radio emissions. Exposure to these radio emissions at a given location on the Earth is dependent on how close that point is to the sun, which can be described by the solar zenith angle (SZA). The ionosphere receives maximum exposure to solar radio emissions where the sun is directly overhead (SZA=0°). Exposure decreases as SZA increases to 90° at the terminator where there is a transition from the sun illuminating the ionosphere from above to below until the SZA reaches roughly 95° and the Earth effectively blocks the sun throughout local night (Turunen et al., 1996).

As the Earth rotates about its spin axis and orbits the sun, riometers move under the same extraterrestrial sources and are therefore expected to observe predictable voltage fluctuations (e.g., the quiet day curve, or QDC) that vary as a function of sidereal time. Sidereal time is scaled based on the Earth's relative rotation relative to fixed stars, as opposed to the sun (e.g. Davies, 1990). A sidereal day is ~4 minutes shorter than a standard solar day and daily variations present in the sidereal day will also be observed on a solar day, with a subtle shift. Deviations in the received signal voltage from the QDC are the result of ionospheric disturbances that cause ionospheric absorption. Absorption (A) is calculated from riometer data by (Browne et al., 1995)

$$\mathrm{A} = 10 \log \frac{V}{V'} \ (dB), \tag{1}$$

where V is the measured voltage, and V' is the undisturbed voltage described by the QDC. Information on deriving the QDC is described in Section 6. During an absorption event the received voltage drops below the QDC and absorption is positive. Bursts of external radio noise, usually from the sun, can cause riometers to measure enhanced voltages which appear as negative absorption.

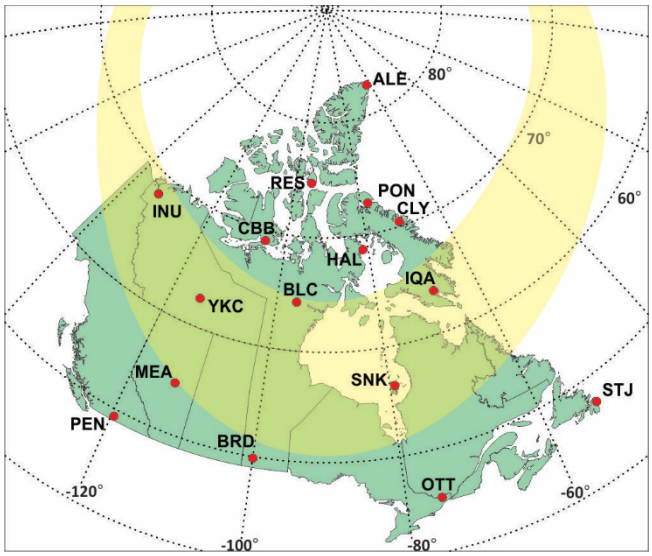

Figure 1: Canadian NRCan riometer station locations (red filled circles) across a geographic reference frame. Yellow shading indicates the modelled location of the discrete auroral oval for Kp=6, calculated 01 June 2020 at 06:00 UT (Sigernes et al., 2011).

Table 1: NRCan riometer station names and abbreviations, geographic latitude, geographic longitude, and altitude adjusted corrected geomagnetic coordinates calculated 15 February 2022 at 00:00 UT. Stations are ordered by descending geographic latitude.

Riometer Station (Name)	Riometer Station (Abbreviation)	Geographic Latitude	Geographic Longitude	Magnetic Latitude
Alert	**ALE**	82.52°	297.73°	86.9°
Resolute Bay	**RES**	74.7°	265.1°	81.9°
Pond Inlet	**PON**	72.68°	282.05°	80.1°
Clyde River	**CLY**	70.48°	291.49°	77.3°
Cambridge Bay	**CBB**	69.1°	255.0°	76.1°
Hall Beach	**HAL**	68.77°	278.75°	76.7°
Inuvik	**INU**	68.3°	226.5°	71.1°
Bakers Lake	**BLC**	64.3°	264.0°	72.5°
Iqaluit	**IQA**	63.7°	291.5°	70.9°
Yellowknife	**YKC**	62.5°	245.5°	68.7°
Sanikiluaq	**SNK**	56.3°	281.0°	65.1°
Meanook	**MEA**	54.6°	246.7°	61.3°
Brandon	**BRD**	49.92°	260.05°	58.6°
Penticton	**PEN**	49.32°	240.37°	55.0°
St. John's	**STJ**	47.6°	307.3°	51.2°
Ottawa	**OTT**	45.4°	284.5°	53.9°

NRCan operates a network of riometers widely distributed across Canada (Danskin et al., 2008; Lam, 2011), as illustrated in Figure 1 and Table 1. Overplotted in Figure 1 as a semi-transparent yellow band is the modelled location of the auroral oval for Kp=6, calculated 01 June 2020 at 06:00 UT according to Sigernes et al. (2011). Here Kp is a geomagnetic activity index based on the magnetic perturbations

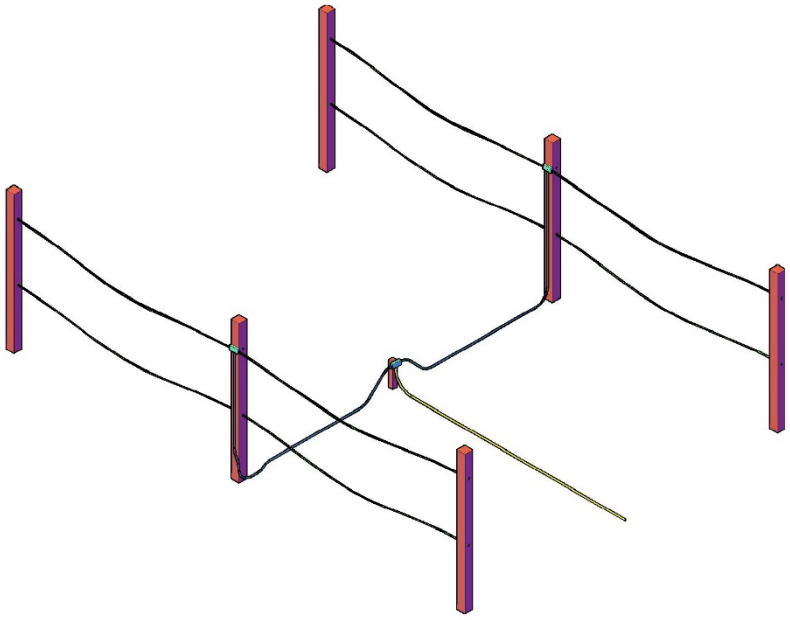

Figure 2: Illustration of the riometer antenna. Dipole elements on either side are connected at the central posts at a balun junction box. The dipoles are joined together in the center of the structure. The dipole elements are paired with a reflecting wire running in parallel underneath.

observed at 13 different magnetic observatories distributed at sub-auroral latitudes across the globe (Menvielle and Berthelier, 1991). Notably, NRCan riometer stations are located poleward of, within, and equatorward of this band in the polar cap, auroral, and sub-auroral regions, respectively. This is significant, as solar disturbances have resultant ionospheric disturbances that impact these regions differently. The widespread distribution of the NRCan riometer network across each region therefore enables observation of the ionospheric impact of a variety of solar phenomena.

NRCan riometer stations described in this work consist of an antenna connected to a *La Jolla Sciences* riometer instrument (Chivers, 1980) tuned to characterize the signal attenuation at 30 MHz. Each wide-beam (~60° beam width) antenna is directed vertically upward to detect signal voltage over a ~100 km diameter circle directly overhead. The antenna consists of a single dual dipole with a reflector wire under each dipole element. The structure consists of six vertical 4 x 4 inch (~10 x 10 cm) wooden posts with four copper wires strung horizontally between them, illustrated in Figure 2. The antenna and reflector wires run in parallel along the 3-post sides (20 ft; ~6.1 m) of the rectangular structure. The antenna wires are 5ft (~1.5 m) above the ground and the reflector wires are 2.5 ft (~76 cm) above the ground. The dipole elements, separated by 14 ft (~4.3 m), are connected by balun connector junctions at the central post of each dipole element in the middle of the structure. The connector in the center of the riometer antenna connects to a cable that runs to the riometer electronics located inside a weather-protected building. Data from the riometer is digitized, timestamped, and stored in a binary format in one-hour increments using an analogue to digital converter and computer attached to the riometer. Data are digitized using 12-bit precision.

Figure 3 is a photograph of the riometer antenna located at Resolute Bay. The overall geometry of the antenna is not crucial, although the wooden posts should be vertical, and the wires should be approximately horizontal. Some sag in the wires is acceptable to accommodate contraction during the winter. The wires must not touch each other, vegetation, or the ground for correct operation. Ideally, the

Figure 3: Photograph of the Resolute Bay (RES) riometer, taken 27 September 2006 by Donald Danskin.

antenna posts should be anchored in the ground to ensure stability. Where that is not possible, an antenna support, as shown in Figure 3 is built.

A variety of data are stored in the binary data files, including the measured riometer voltage. Voltage, in units of mV, is sampled ~60 times per second, but downsampled to one second resolution using the median voltage per second. In addition to the voltage, the range of voltage per second, calculated as the maximum voltage minus the minimum voltage recorded in a second, and the number of samples are stored. The range serves as a pseudo error to the voltage values. A riometer alternates between regular calibration periods where the instrument is receiving signal from a calibration signal, and normal operation where the instrument receives signals only from external sources. NRCan riometers have 24 calibration periods per day, alternating between one of four fixed signal levels. Calibration periods are characterized by a step function in the voltage data to a roughly constant value. The step function causes the range to spike at the start and end of the calibration period and maintain a smaller value than is observed during non-calibration periods. A binary calibration flag is stored to indicate when the instrument is in calibration or external listening mode. Voltage, number of samples, and range values are all positive numbers, though voltage can take on small negative values (e.g. as low as ~ -0.2 V) during calibration periods.

Raw binary data are converted into a standardized American Standard Code for Information Interchange (ASCII) format to create a data product for dissemination. Three ASCII data products have been developed: Level 1, Level 2, and Level 3. The Level 1 data file is a quick organization of the original binary data for a given station into a single ASCII file for each day. Header information includes important meta data such as the station name and abbreviation (see Table 1), network array name, geodetic latitude, geodetic longitude, date of observation, day of year, and additional information describing the contents of the data arranged in columns with entries for time (s), voltage (mV), number of samples per second, range (mV), and calibration flag. Level 1 data files replicate the contents of the binary data (i.e., the 'raw' data) and as such can have gaps where data from multiple binary files are merged together and calibration periods are not always accurately marked. Level 1 data products are not discussed further in this report.

Level 2 data files, pictured in Figure 4, are also generated directly from the binary data files and represent a more consistent and uniform data product for dissemination. Unlike binary or Level 1 data files, Level 2 data files contain QDC voltage (mV) corresponding to the date represented by the file, and absorption at

```
|Station Name:                                Ottawa
|Station Tag:                                    ott
|Station Array:                                nrcan
|Geodetic Latitude:                          45.4000
|Geodetic Longitude:                         284.450
|Date:                                      2022-01-22
|DOY:                                           022
|Voltage is the median voltage in a second, with
|the number of samples in a second recorded, as
|well as the range of the voltages measured. Cal
|is set to one when the riometer is calibrating,
|and to zero otherwise. Quiet Day Curve(QDC)
|Voltages are calculated automatically and
|absorption values are calculated using the ratio
|between the QDC voltage and the measured voltage.
|
|Time      Volts Samples  Range Cal    QDC  Absorp
00 00 00   5.085      78  0.012   0  4.618  -0.418
00 00 01   5.066      80  0.022   0  4.618  -0.402
00 00 02   5.054      79  0.010   0  4.618  -0.392
00 00 03   5.057      80  0.007   0  4.618  -0.394
00 00 04   5.060      80  0.021   0  4.618  -0.397
00 00 05   5.085      81  0.016   0  4.618  -0.418
00 00 06   5.077      80  0.026   0  4.618  -0.411
00 00 07   5.048      80  0.018   0  4.618  -0.386
00 00 08   5.045      80  0.006   0  4.618  -0.384
00 00 09   5.054      80  0.018   0  4.618  -0.392
00 00 10   5.061      79  0.011   0  4.618  -0.398
00 00 11   5.049      80  0.018   0  4.618  -0.387
```

Figure 4: Example of a Level 2 riometer data file for the OTT riometer station on 22 January 2022.

30 MHz, in dB. Level 2 data files are organized by date, according to Universal Time (UT), with one file per day, and one entry for each second of the day. Fill values of -9 or -9.000, depending on the format of the data, are used to fill data for missing time entries. Figure 4 is a screen capture of a Level 2 riometer data file for the OTT riometer station on 22 January 2022. Header information is identical to that included in a Level 1 data file and includes the station name, abbreviation, network array name, geodetic latitude, geodetic longitude, date of observation, day of year, and additional information describing the columns of data. The first column represents time with two-digit entries for year, month, and day. Voltage, in mV, is recorded in column 2. Columns 3 and 4 indicate the number of samples within the 1 second interval represented by each line, and the range of values in a sample, in mV, respectively. The 'Cal' column contains the calibration flag indicating whether the riometer was collecting data during a calibration period; one during calibration periods, and zero otherwise. The calibration flag is also set to zero for entries corresponding to missing data. QDC voltage, in mV, is provided in column 6. The final column is the absorption calculated from the QDC and voltage columns using equation (1). Each file contains 864000 lines of data representing each second of the day, with additional lines for the header. Level 2 data files are generated automatically.

Level 3 data files are almost identical to the Level 2 data files but include an extra column of integer value quality flags that provide additional information about the data. The main purpose of the quality flags is to indicate data reliability; riometers are very sensitive instruments and the data are easily contaminated, for example, by a variety of noise sources attributed to weather (e.g., freezing rain, thunderstorms), flora or fauna interfering with the antenna, or changes in the instrumentation or nearby instrumentation. Level

3 data files have a preliminary and definitive format. Data in the preliminary format are flagged based on features that can be evaluated automatically. Data in the definitive file format include more descriptive flags assigned through careful evaluation of the data by an operator. Quality flag values, whether they are defined automatically or by an operator, and a description of the quality flags are provided in Table 2.

Several quality flags are assigned through an automated routine to create the preliminary Level 3 absorption file. By default, data are assumed to be reliable, or of 'good' quality, and are assigned a flag of '1'. Where data are of good quality, and absorption is also observed, a quality flag of '23', '29', or '31' is used to indicate the absorption is most likely due to 'shortwave fadeout', 'auroral absorption', or 'polar cap absorption'. Section 4 provides a detailed description of the automated absorption flagging routine.

Table 2: Riometer quality flags, label, method of assignment (automatic or by operator), and description.

Number	Label	Method	Description
1	good	default	Data are automatically assigned a quality flag of '1' prior to any additional processing.
2	bad / fill value	operator	An operator assigns a quality flag of '2' if the data are clearly of poor quality when the exact source of the error is unclear or due to multiple phenomena.
3	questionable	operator	Data exhibit clear trends, but there is some noise or error in the data. This data should be carefully inspected by the user before blind-processing.
5	spike	automatic	See Section 6.
7	environmental	operator	Examples include thunderstorms, which appear as isolated periods of noise that often drift between adjacent stations, and freezing rain which appears as an unexplained period of absorption lasting hours (or more) in conjunction with near zero temperature and precipitation at the riometer station.
11	instrument error	operator	Identified by periods of noisy erratic data or step jumps in the voltage. Attributed to, for example, aging components, water in the connector, or damage to or slack in the antenna wires.
13	QDC error	operator	QDC does not accurately represent the data, but there is no other error or absorption observed.
17	radio noise	operator	Appear as sharp spikes of positive voltage. Short radio bursts appear as spikes but are observed by multiple dayside stations. Longer periods of radio noise are often observed across the dayside for prolonged periods of time and can recur for extended periods of time.
19	calibration	automatic	Periods where the riometer is calibrating.
23	shortwave fadeout	automatic	See Section 4.1.
29	auroral absorption	automatic	See Section 4.2.
31	polar cap absorption	automatic	See Section 4.3.
37	voltage saturation	automatic	See Section 3.

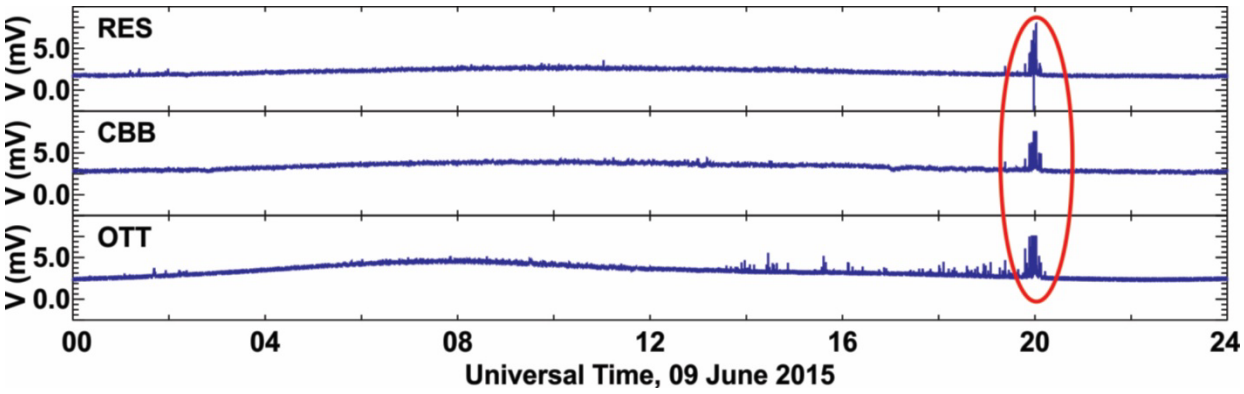

Figure 5: Voltage for a selection of riometer stations on 09 June 2015. Positive voltage spikes indicated by the red oval at ~20 UT are caused by a radio noise burst.

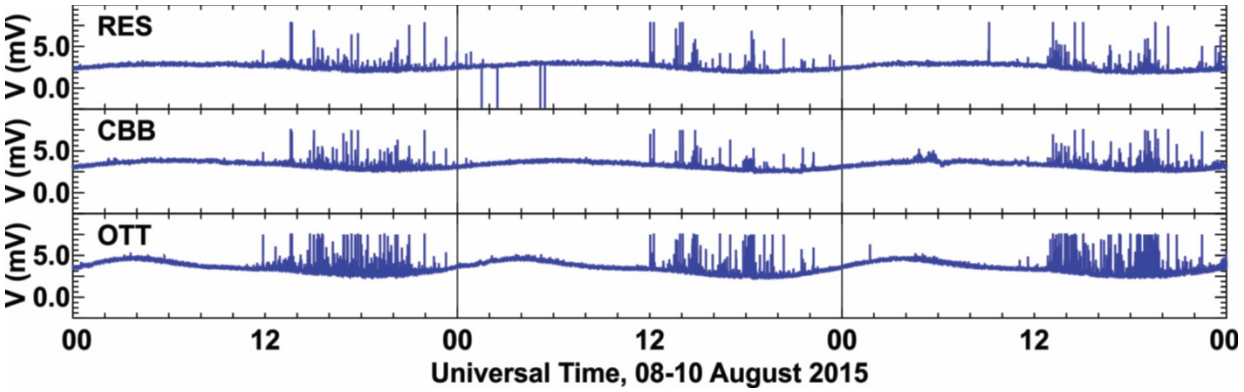

Figure 6: Voltage for a selection of riometer stations on 08-10 August 2015. Positive voltage spikes are observed 12-22 UT each day due to a radio noise storm.

Next, data spikes are identified following the despiking procedure described in Section 3 and assigned a quality flag of '5'. Finally, data collected during calibration periods, which therefore do not represent ionospheric absorption are automatically flagged with a quality flag of '19'. Note that in the automatic flagging algorithm, calibration flags have precedence over spike flags, and spike flags have precedence over absorption flags.

Not all features can be identified automatically, and additional adjustments are often made by an operator after the preliminary data file is produced to identify noise sources in the data. The three main types of operator-flagged noise sources are radio noise (quality flag = '17'), environmental noise (quality flag = '7'), instrument error (quality flag = '11'), and errors caused by an ill-fitting QDC (quality flag = '13'). Where an operator cannot pinpoint the source of unreliability of the data, or where the data quality is not clear the operator may also assign a quality tag of '2' or '3' to indicate 'bad' or 'questionable' data.

Radio noise originates from the sun and is observed by riometers on the sunlit side of the Earth. Radio noise emissions are characterized in riometer data by positive voltage spikes. Signatures are seen across a wide range of latitudes and are typically stronger at lower latitudes and on the dayside (i.e. , closer to the sub-solar point). Signatures are therefore concentrated on the dayside and are stronger and more frequent during the summer months. Voltage spikes due to radio noise can be isolated (radio noise burst), or repeatedly observed on the dayside of the Earth for several days extending to weeks or months in some cases (radio noise storm). A radio noise burst is seen across three representative stations of varying latitude in Figure 5 at ~20 UT on 09 June 2015. Figure 6 shows a longer period of radio emissions observed between 12 and 22 UT each day 08-10 August 2015. This activity was observed with varying levels of

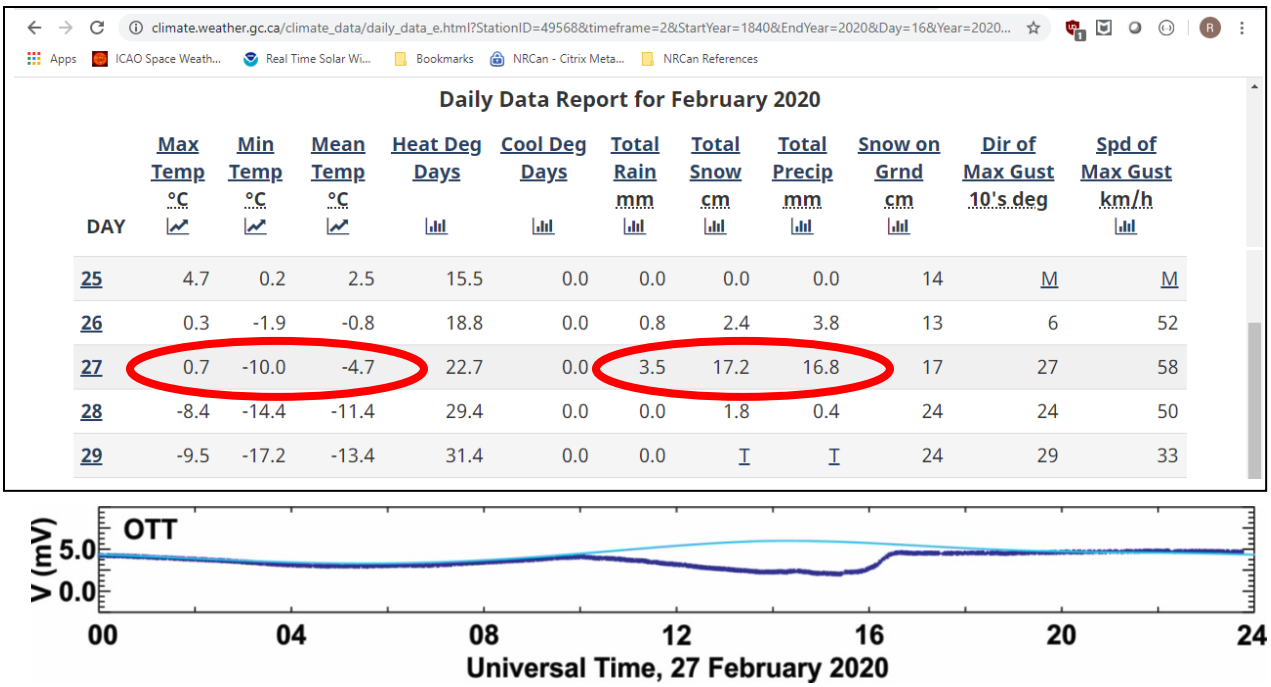

climate.weather.gc.ca/climate_data/daily_data_e.html?StationID=49568&timeframe=2&StartYear=1840&EndYear=2020&Day=16&Year=2020...

Apps | ICAO Space Weath... | Real Time Solar Wi... | Bookmarks | NRCan - Citrix Meta... | NRCan References

Daily Data Report for February 2020

DAY	Max Temp °C	Min Temp °C	Mean Temp °C	Heat Deg Days	Cool Deg Days	Total Rain mm	Total Snow cm	Total Precip mm	Snow on Grnd cm	Dir of Max Gust 10's deg	Spd of Max Gust km/h
25	4.7	0.2	2.5	15.5	0.0	0.0	0.0	0.0	14	M	M
26	0.3	-1.9	-0.8	18.8	0.0	0.8	2.4	3.8	13	6	52
27	0.7	-10.0	-4.7	22.7	0.0	3.5	17.2	16.8	17	27	58
28	-8.4	-14.4	-11.4	29.4	0.0	0.0	1.8	0.4	24	24	50
29	-9.5	-17.2	-13.4	31.4	0.0	0.0	T	T	24	29	33

Figure 7: (Upper) Daily weather report for 25-29 February 2020. On the 27th temperatures were near 0° Celsius combined with a notable amount of precipitation, indicative of freezing rain. Source: www.weather.gc.ca. (Lower) Voltage (purple) and quiet day curve (blue) for the Ottawa (OTT) riometer on 27 February 2020. High levels of apparent absorption observed on the 27th, indicated by a drop in voltage compared to the quiet day curve, are due to freezing rain accumulating on the antenna.

severity over a wide range of stations on the dayside during each of the three days shown. This example of a longer duration dayside recurring period of radio noise is an example of a radio noise storm.

Environmental phenomena contributing to noise in riometer data signatures are freezing rain and electrical storms. Freezing rain on the antenna can cause a decrease in voltage that resembles increased absorption. However, such a feature will typically only be observed in one station, can happen at any time of the day, and can occur at any latitude. Incidents due to freezing rain are evaluated by eliminating absorption due to other causes (examining the solar proton flux, solar X-ray flux, geomagnetic activity levels, or features present in data for other nearby stations) and by examining the local weather for the site in question to determine if freezing rain was either reported or likely (temperatures near 0° Celsius combined with precipitation). For an example see Figure 7. Interference from electrical storms appear as radio noise with spiky positive voltage excursions. Unlike radio noise storms, electrical storms are generally observed by one station at a time, but may drift from one station to the next, depending on their proximity, as is demonstrated in Figure 8.

Instrument error can be more challenging to distinguish, and other sources of absorption should be eliminated first. Sources of instrument error include, but are not limited to, moisture in the connector, sagging antenna wires or antenna poles, aging components, vegetation encroaching on the antenna, and interference by animals. One obvious signature is a sharp step in voltage from a value that closely matches the QDC to a value that follows the trend of the QDC, but is consistently offset, such that a step function is produced in the absorption data. This is an instrument malfunction, likely due to a faulty connector.

Although care is taken to ensure an accurate QDC, it is possible that the algorithm described in Section 6 will produce a poor fit, which is generally characterized by regular diurnal peaks in the absorption data.

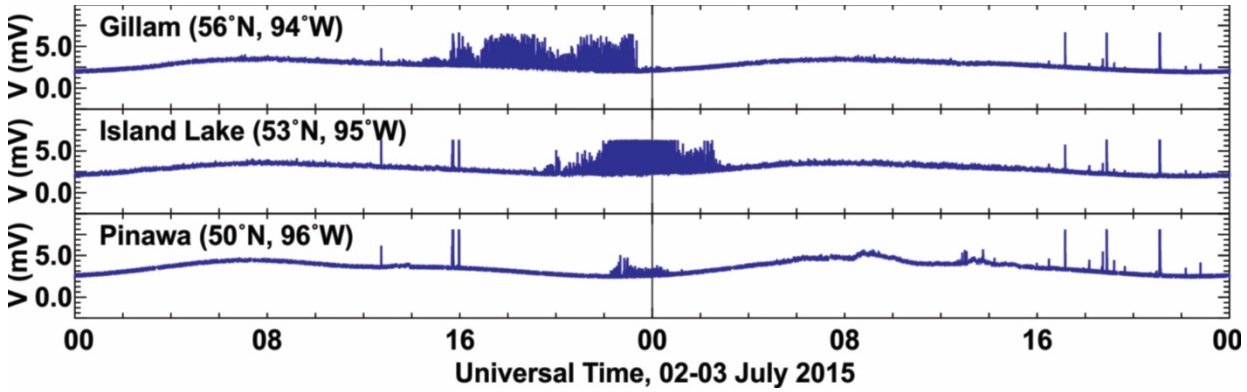

Figure 8: Voltage for three riometer stations operated by the University of Calgary 02-03 July 2015. The riometer station names and geographic coordinates are indicated. A radio noise burst at ~16 UT on 02 July 2015 is immediately followed by a thunderstorm at the Gillam station, which is observed ~4 hours later at the Island Lake station and, to a lesser extent, the Pinawa station.

This is different from a polar cap absorption signature which will only be observed when the >10 MeV solar proton flux is elevated, with a prominent enhancement on the dayside which diminishes according to trends in the >10 MeV solar proton data.

The operator-defined flags described in this Section are not considered in the real-time data analysis described in the following sections. However, they are useful for processing of archived data for event studies, statistical analysis, and model development.

3. Algorithm

This section describes the algorithm for processing riometer data in near real-time. This algorithm (1) derives an accurate QDC based on downsampled 1-minute data, (2) creates Level 3 data files at a 1-second resolution, and (3) generates near real-time plots (e.g., live plotting) of the data. For all three procedures, temporary data from previous runs of the algorithm are loaded. Data obtained from a new run of the algorithm is determined and processed as described below. Figure 9 is a flowchart indicating the flow of data to create each of the three data products. The left-side plot describes generation of the QDC and creation of the Level 3 data file, and the right-side plot describes generation of near real-time data plots.

The first step in all procedures is to apply automatic quality flags to the 1-second Level 2 data. By default, the quality flag for the 1-second data is set to '1' for 'good'. Data corresponding to fill values are assigned quality flags of '2' for 'bad' and are not used in the calculations described throughout this report. Quality flags for data collected during calibration periods are set to '19' for 'calibration'.

Following this simple filter to set the quality flags, the 1-second data are despiked. 'Good' quality data are first smoothed using a boxcar average over 120 seconds. The absolute value of the difference between the smoothed data and measured data is determined. Data with a difference more than two standard deviations from the mean are flagged as 'bad' along with any data point within +/- 10 seconds of the spike. The 10-second buffer was empirically determined by observing the use of a range of buffers up to 60 seconds and balancing the removal of spike signatures with the removal of an excess of valid data.

Next, saturated voltage values from solar radio noise are removed. These are identified in two ways. First, the maximum voltage values in five-minute intervals are determined. The first-order center difference is

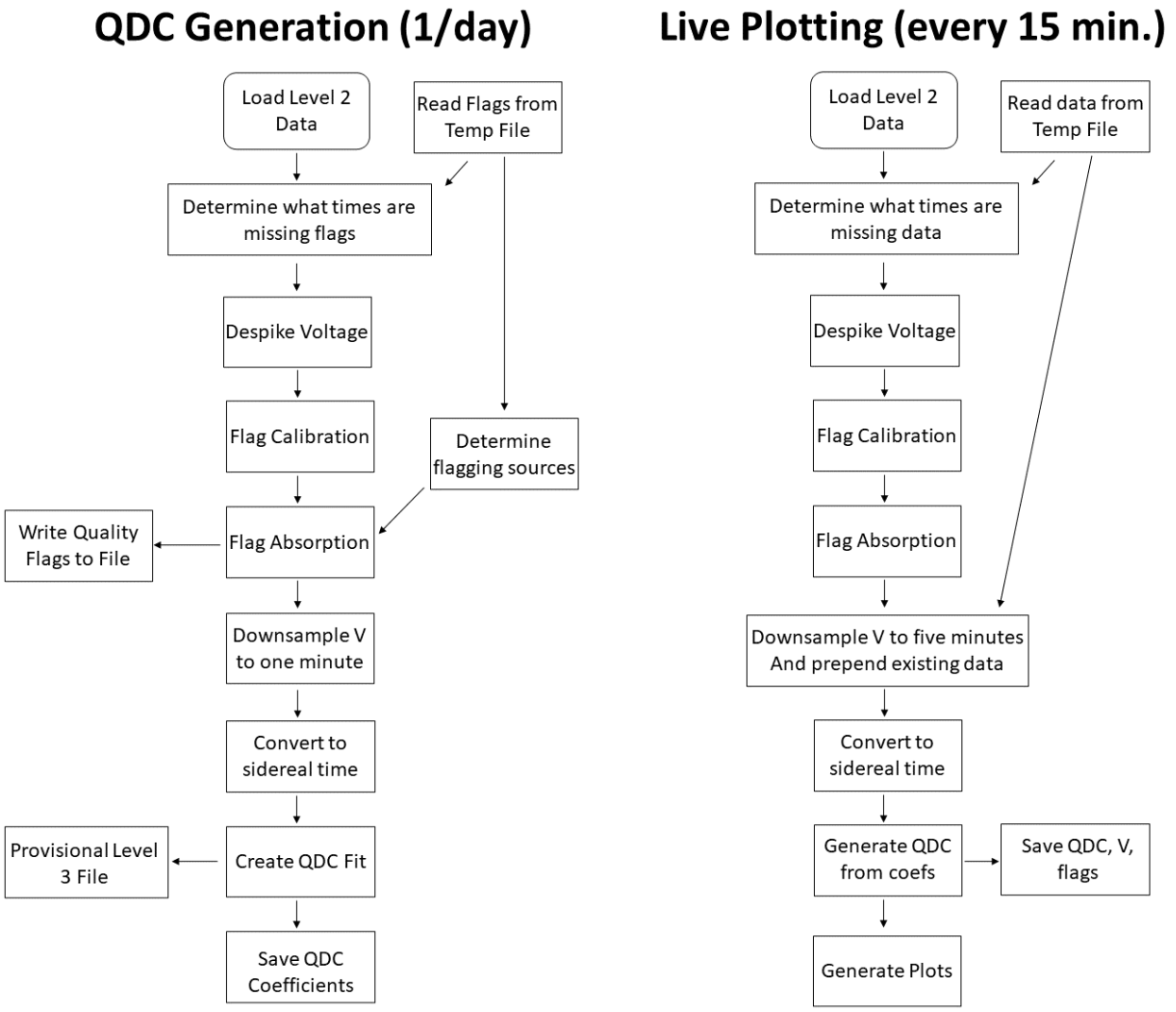

Figure 9: Flowchart illustrating near-real-time processing of riometer data and quiet day curve calculation. As indicated, the quiet day curve, used for calculating absorption, need only be calculated once per day.

calculated for the maximum values. A threshold is then applied, where differences below a threshold of 0.04 mV are assigned a flag of '37' for 'saturation'. Additionally, voltage values above the mean plus one standard deviation for the last fourteen days are also flagged '37' for 'saturation'. Automatic quality flagging is now complete.

Absorption is calculated from 1-second voltage data using the QDC corresponding to the calendar day of observation. QDC calculation requires quiet periods be isolated by first identifying times when absorption is expected. Three types of absorption are considered: shortwave fadeout, auroral absorption, and polar cap absorption. Thresholds for describing when each type of absorption is expected for individual riometer stations are described in Section 4. The absorption flags are saved in a temporary file for use in future runs of the QDC algorithm. One second voltage data, quality flags, and absorption flags are downsampled to a one-minute interval to smooth noise in the data and reduce processing time according to descriptions in Section 5, and converted to sidereal time to evaluate the QDC, as described in detail in Section 6. In NRCan's implementation, QDC coefficients are generated at the start of each day. One-

second riometer voltages are combined with the daily QDC coefficients to generate preliminary Level 3 data files.

Near real-time data processing should occur on a regular basis (e.g., every 5, 10, or 15 minutes). Although the data are processed quickly, buffering the data to display plots is comparatively slow, and it is suggested that data be downsampled to no less than a 5-minute resolution for live plotting.

Currently, after calculating the day's QDC, the algorithm then saves the previous day's 1-second data with updated flags as a provisional level 3 file, with a similar format to that described in Section 2, though with automatically generated data quality and absorption flags. Additionally, the saved QDC coefficients are stored as metadata.

4. Flagging absorption

Various space weather parameters are evaluated to determine whether or not absorption due to shortwave fadeout, auroral absorption, or polar cap absorption is likely. Quality flags during periods of absorption are assigned the values described in Table 2. Data flagged in this way are still considered to be of good quality. Flagging is necessary to mark that data for exclusion in the QDC-determination algorithm.

4.1. SHORTWAVE FADEOUT

Shortwave fadeout is caused by increased photoionization on the dayside of the Earth due to a solar X-ray flare (e.g., Mitra, 1974). Fiori et al. (2022a) show that the relationship between absorption at 30 MHz (A_{30}), the 0.1-0.8 nm solar X-ray flux (F), and the solar zenith angle (SZA) of the impacted region is given by:

$$A_{30} = \left[12080 \left(\frac{m^2 dB}{W}\right)\right] F \cos(SZA) \text{ (dB)}. \quad (2)$$

Absorption is strongest when the sun is directly overhead and falls off with increasing proximity to the solar terminator. Canada is therefore more sensitive to shortwave fadeout in the sub-auroral region, especially on the dayside.

Shortwave fadeout is flagged by identifying periods where A_{30} is predicted to be > 1.0 dB based on equation 2, calculated at the coordinates of the riometer station under evaluation. As an example, to determine the minimum solar X-ray flare likely to impact Canada, consider the maximum SZA at 42° geographic latitude, which is roughly the low-latitude extent of Canada. At this latitude, SZA ranges from roughly 18° to 161° over the course of a year, and the minimum solar X-ray flux expected to cause 1 dB absorption is therefore 8.7×10^{-5} Wm^{-2}, or an M8.7 solar X-ray flare. Solar X-ray flux is available in near real-time from the National Oceanic and Atmospheric Administration (NOAA) Space Weather Prediction Center (SWPC) JSON service (https://services.swpc.noaa.gov/json/goes/primary/xrays-1-day.json).

4.2. AURORAL ABSORPTION

Energetic electron precipitation causes ionization in the D-region auroral zone ionosphere leading to auroral absorption (e.g., Baker et al., 1981; Hargreaves, 1969; Newell et al., 2001). Auroral absorption is strongest in the midnight sector, but also peaks in the pre-noon sector (e.g., Hargreaves, 2010; Kavanagh

et al., 2004b, Basler, 1963; Driatsky, 1966). Events typically last on the order of 1-3 hours but can be as long as ~12 hours in extreme cases (Hargreaves, 2010; Fiori et al., 2022b). Auroral absorption enhancements follow trends in geomagnetic perturbations (e.g., Hargreaves, 1966; Kellerman and Makarevich, 2011; Rodger et al., 2013). It is therefore common to parameterize auroral absorption according to geomagnetic activity indices, such as the Kp or Ap index (e.g. Foppiano and Bradley, 1983, 1984; Hartz, 1963; Hargreaves, 1966; 2007; Hargreaves and Cowley, 1967; Hargreaves et al., 1987; Holt et al., 1961; Kavanagh et al., 2004b; Rogers et al. 2016). At present, the Kp index is used by the International Civil Aviation Organization (ICAO) as a threshold to indicate moderate (Kp=8) and severe (Kp=9) geomagnetic activity (ICAO, 2018; 2019). Fiori et al. (2020) examines the relationship between the hourly range of absorption and the Kp index during periods of auroral absorption and concludes there is a general linear relationship between absorption and Kp for Kp ≤ 4. Increased variability in the data for Kp > 4, degrades the apparent relationship. They attribute the disagreement to three sources: strong variability in absorption over the 3-hour interval for which Kp is evaluated, disagreement between the location of sub-auroral stations contributing to the Kp-index and energetic particle precipitation into the high-latitude region, and fewer events where Kp > 4. They also point out inconsistencies in using a global geomagnetic index to characterize a highly localized phenomenon. Fiori et al. (2020) show that there is a better agreement between trends in hourly range of absorption and hourly range of the magnetic field where co-located observations exist.

Fiori et al. (2020) determined that the AE index is a much better indicator of global-scale auroral zone activity. The AE index describes the geomagnetic response to changes in the auroral electrojet based on an examination of the upper and lower envelopes of the horizontal magnetic field observed by selected magnetometer stations distributed worldwide at auroral latitudes (Davis and Sugiura, 1966). However, since the AE index is not publicly available in real-time, a proxy index (AE_{proxy}) based on the hourly range (HR) of the magnetic field observed by NRCan auroral-zone riometers is instead considered. For more information on how HR is evaluated for an individual magnetometer station see Hruska and Coles (1987). To determine AE_{proxy}, the relationship between HR and AE was first examined. A linear regression between the maximum HR derived from auroral zone riometers (HR_{AUR}) located at Sanikiluaq, NU (SNK), Fort Churchill, MB (FCC), Yellowknife, NWT (YKC), Baker Lake, NU (BLC), Iqaluit, NU (IQA), and Cambridge Bay, NU (CBB) for 2010-2018 was compared to the maximum hourly AE index, yielding the following linear relationship:

$$\mathrm{AE}_{\mathrm{proxy}} = \frac{\mathrm{HR}_{\mathrm{AUR}} - 31.84}{0.3972}\ (\mathrm{nT}). \tag{3}$$

To flag auroral absorption AE_{proxy} is calculated every 15 minutes using equation (3) where HR_{AUR} is calculated based on the hourly range observed over the last 60 minutes. Fiori et al. (2023) identified a threshold of 0.5 dB absorption at 30 MHz for characterizing impacts to high frequency radio systems in the < 20 MHz range typically used for communications. According to Fiori et al. (2020), this corresponds to an AE index of 800 nT. A threshold of AE_{proxy}= 800 nT is therefore used to identify periods of possible auroral absorption for flagging.

4.3. POLAR CAP ABSORPTION

Polar cap absorption is caused by the precipitation of energetic protons following a solar eruption and accompanying solar proton event (e.g., Kavanagh et al., 2004a; Neal et al., 2013). The solar protons are accelerated to near-relativistic speeds reaching the Earth after ~1-3 hours where they penetrate the high-latitude D-region, extending poleward of ~60° magnetic latitude in both the northern and southern

hemispheres. During such events, absorption can be elevated for periods on the order of hours to days, with the strongest impacts observed on the dayside. Solar emissions where the >10 MeV solar energetic proton flux exceeds 10 pfu are known as solar proton events, and typically lead to polar cap absorption. A threshold of 10 pfu in the >10 MeV solar energetic proton flux is therefore used to identify periods of potential polar cap absorption.

During these periods absorption is mostly likely to be enhanced on the dayside, particularly at auroral zone and polar cap riometer stations. Enhancements may not extend to the sub-auroral, twilight, or nightside regions. Solar proton data are available in near-real time from the NOAA SWPC JSON service (https://services.swpc.noaa.gov/json/goes/primary/integral-protons-1-day.json).

4.4. ABSORPTION FLAG USE

The above-described absorption flags are associated with each 1-second data period for the Level 2 data ingested into the algorithm. These are saved as preliminary level 3 files, which contain the automated flags listed in Table 2. For periods not flagged as 'bad' quality, or associated with calibration, if a single type of absorption is present, its corresponding value in Table 2 is assigned. For periods with multiple absorption types associated with them, only a single flag value is assigned. For this case, precedence is given by shortwave fadeout over auroral absorption over polar cap absorption. This 1-second flag product is used in Section 5 to generate downsampled flag products, to calculate QDCs and generate near-real time riometer plots.

5. Downsampling riometer data

Level 2 riometer data are available in a 1-second resolution. Although this fine resolution is sufficient to show small-scale structures in absorption, it can be susceptible to noise, creates large output plots, and can take a long time to process. To speed up calculations where such a fine resolution is not required, to reduce noise, and to match the resolution of complementary data sets, it can be necessary to downsample the data to a more manageable resolution. For example, a 1-minute downsample is used for calculation of the quiet day curve coefficients, as seen in Section 6. To evaluate the data operationally a 5-minute resolution is recommended to create reasonably sized multi-station plots and data streams. The live plotting algorithm described in Section 7 uses 5-minute resolution downsampled data.

Figure 10 demonstrates the use of a 5-minute median to downsample riometer data. Data are shown for 20-22 October 2022 for the OTT riometer station. The upper panel shows the 1-second data. Minuscule variations in the voltage data (dark blue) are exaggerated in the absorption curve (green). In the lower plot the absorption and voltage data are each downsampled using a 5-minute median. The effect of downsampling is to smooth noise in both the voltage and absorption curves. Note that calculating the downsampled absorption from 1-second data is not a significant computational burden; most of the runtime is spent in file handling for riometer and supplementary absorption products.

For QDC determination, the quality flags and absorption flags are downsampled using a simple algorithm. Downsampled flags characterize the data as 'good', 'bad', or 'questionable' based on thedata quality (i.e. calibration and spikes). For each downsampled period, the fraction of data characterized by a good data quality flag determines the period's classification. If ≥75% of the 1-second data within the downsampled period is flagged as good quality, the downsampled data point is flagged as good quality. If 25-75% of the 1-second data is flagged as good quality, the downsampled data point is flagged as 'questionable' quality.

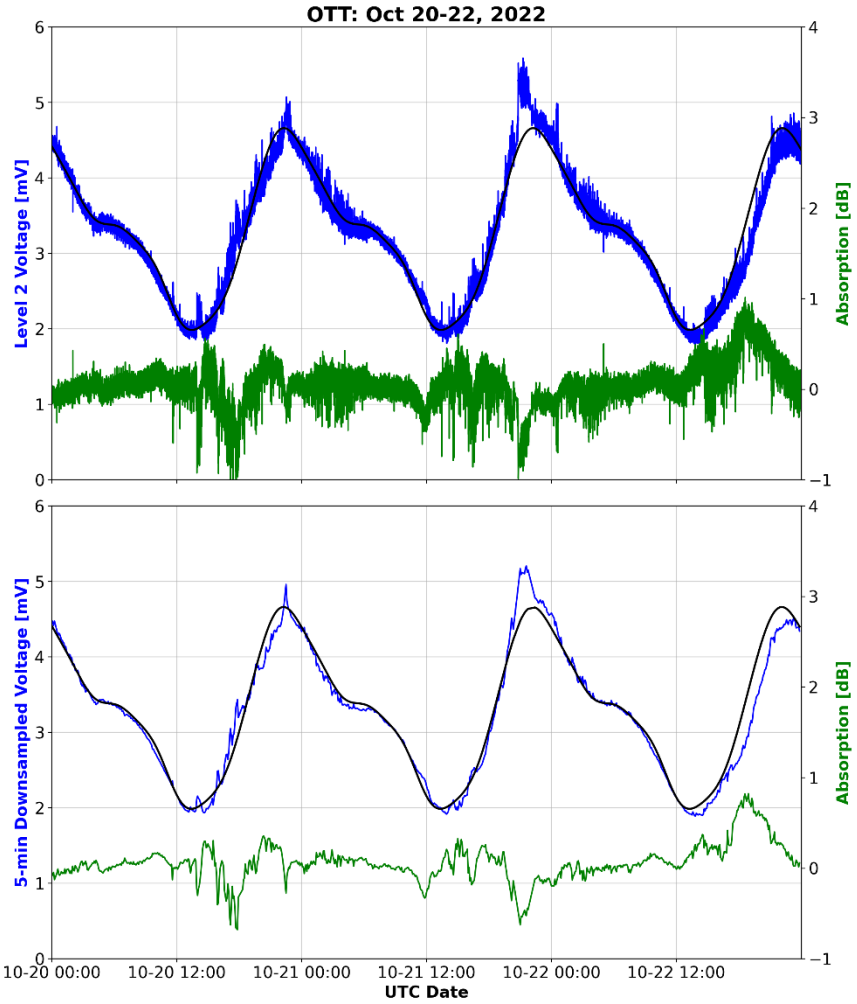

Figure 10: Riometer voltage (dark blue), QDC (black) and absorption (green) for the OTT riometer for 20-22 October 2022. The upper panel shows the 1 s cadence data, and the bottom panel shows 5-minute downsampled data. All data are plotted regardless of data quality or absorption status.

If less than 25% of the 1-second data is flagged as good quality, the downsampled data point is flagged as 'bad' quality. This downsampled flag does not include information on absorption, only the proportion of the data flagged as being of suspect quality or containing calibration periods.

An additional identifier is used for each downsampled period, which identifies the type of absorption associated with that period. For each downsampled period, if any absorption is flagged in the input 1-second data, it is flagged for that type of absorption. For periods with multiple types of absorption, the type flagged for the majority of the period is used. For periods with equal amounts of different types of absorption, priority is given (in order) to shortwave fadeout, then auroral absorption, and finally polar cap absorption.

In summary, each downsampled point has two flags associated with it – one for overall quality, and one to identify periods of absorption. Both downsampled quality flags are used to determine inclusion of the data in the QDC, and can be used, for example, to create a visual interpretation of the data quality and likelihood of ionospheric absorption for live-plotting.

6. Determining the quiet day curve (QDC)

A QDC is determined for a given day and station by analyzing the measured voltage collected over the two-week period immediately preceding the day being fit. For each day, good-quality 1-second data are first despiked (using methods described in Section 3), flagged for periods of absorption (as outlined in Section 4), and downsampled to a 1-minute resolution (as described in Section 5). The downsampled quality flags are used to remove 'bad' and 'questionable' data from the data set. Additionally, downsampled periods flagged as containing any absorption are excluded from QDC fits. These two downsampled flags (data quality and absorption) provide an ability to isolate quiet periods for fitting quiet day variations. Times associated with the remaining 1-minute data are converted from Universal Time to sidereal time. The remaining data are then binned for each minute of one sidereal day, and the median value is determined for each bin. These median values for one sidereal day are repeated side-by-side-by-side to create a 3-day continuous data set and fit using a 6th order harmonic expression:

$$\mathrm{QDC} = \mathrm{A}_0 + \sum_{\mathrm{n}=1}^{6} \mathrm{A}_\mathrm{n} \sin(\mathrm{n}\omega\mathrm{t} - \varphi_\mathrm{n}) \quad (4)$$

where n is the order of sinusoid to be fit, ω is the fundamental angular frequency for the fitted sidereal day, t is time, A_n is the nth order fitted scaling coefficient, and φ_n is the nth order phase shift coefficient. The three-day stacking is necessary to create a continuous baseline that is well behaved at the start and end of the day. If <25% (determined experimentally) of the data is available, of good quality, and has no anticipated absorption, then the fitting is aborted and the QDC for the previous good day is applied to the data set. It is possible for stations in good working order to not have enough available data for QDC fitting during, for example, a long solar proton event. In addition to the two-week harmonic fit described above, a vertical offset adjustment is made using the previous two days of data. This adjustment adjusts the A_0 term using the most recent two days of riometer data, to minimize the difference between the QDC mean and measured voltage mean values. This was found to be necessary to correct for daily variations in antenna response due to changing environmental factors. This correction factor is only applied in instances where there is >50% data with no absorption and no data quality issues.

Smoothing data in the QDC baselining and fitting procedure, in combination with the noise often observed in riometer data, even during quiet periods, makes a high level of data precision impossible. Absorption data is accurate to 0.1 - 0.2 dB (Foppiano and Bradley, 1984; Kavanagh et al., 2004a; Fiori et al., 2020). Despite this, it is possible to evaluate QDC performance through statistical analysis.

One method of evaluating the success of the QDC algorithm is by evaluating the agreement between the QDC and the measured voltage. During quiet periods, the voltage curve should completely overlap with the QDC voltage. Quantifying the correlation between measured riometer voltage and calculated QDC voltage provides a useful metric by which the accuracy of the QDC calculation algorithm can be evaluated. Conversely, the deviations from the QDC for absorption flagged periods provide information on the extent to which the absorption flagging criteria are over or under-flagging periods of absorption. Similarly, the accuracy of data quality flagging can be assessed through the prevalence of deviation of measured voltages from QDC voltages for those identified 'bad' periods.

To demonstrate, QDC baselining was performed for 04-18 September 2017. Figure 11 shows (upper panel) voltage data, the QDC, and (lower panel) calculated absorption for Cambridge Bay, NU (CBB). This time frame contains an extended period of polar cap absorption (red) and auroral absorption (purple), as

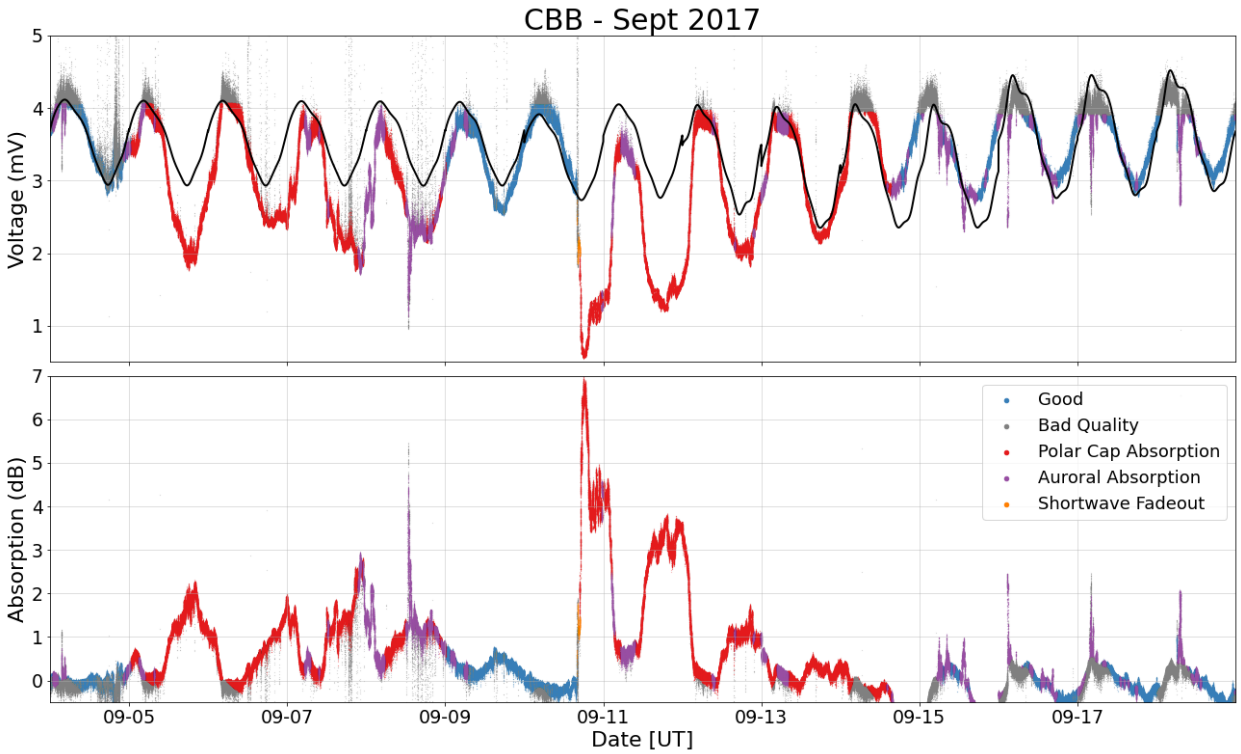

Figure 11: Riometer voltage and absorption for 04-18 September 2017 at Cambridge Bay, NU. Data is color-coded to indicate 'good' (blue) quality data, 'bad' (grey) quality data, polar cap absorption (red), auroral absorption (purple), or shortwave fadeout (orange). Top: Measured voltage and QDC voltage (black line) for the period of interest. Bottom: Calculated absorption for the same period.

well as a brief period of shortwave fadeout (orange) late September 10th. Each day the QDC curve fitting algorithm was applied. However, based on the predominance of expected periods of absorption, the QDC algorithm aborted calculating a vertical offset 05-09 September and September 11-16, 2017, instead using the QDC calculated from the previous 14 days of data. (This is also shown in the shift in the QDC from 04 September to 05 September in the OTT riometer data in the forthcoming Figure 13.) Despite extended periods of absorption, the relatively long window for fitting (2 weeks versus 2 days), and permissive threshold for conducting the fit (>25% of the data is available, of good quality, and has no anticipated absorption with a vertical correction factor being applied in instances where > 50% of the data is of good quality data with no absorption) means that updated QDCs were still calculated, though using a relatively restricted fitting data set. During automatically determined periods of expected polar cap absorption, auroral absorption, and shortwave fadeout, the measured voltage drops below the QDC and the calculated absorption is enhanced. Conversely, during periods expected to be quiet, or 'good', the measured voltage more closely matches the QDC. Sharp fluctuations in the QDC around daily transitions are due to changes in the QDC fit coefficients, primarily the vertical offset.

Figure 12 shows a comparison between the QDC voltage and the measured voltage for differently flagged periods for the CBB voltages plotted in Figure 11. The upper panel shows quiet periods where the data are of good quality and are not expected to contain absorption. The middle panel shows periods where the data are of good quality and are expected to observe absorption based on the automatic detection algorithm described in Section 4. The lower panel represents all periods where the data are of poor quality, regardless of absorption status. In this analysis only automatic data quality flags are considered.

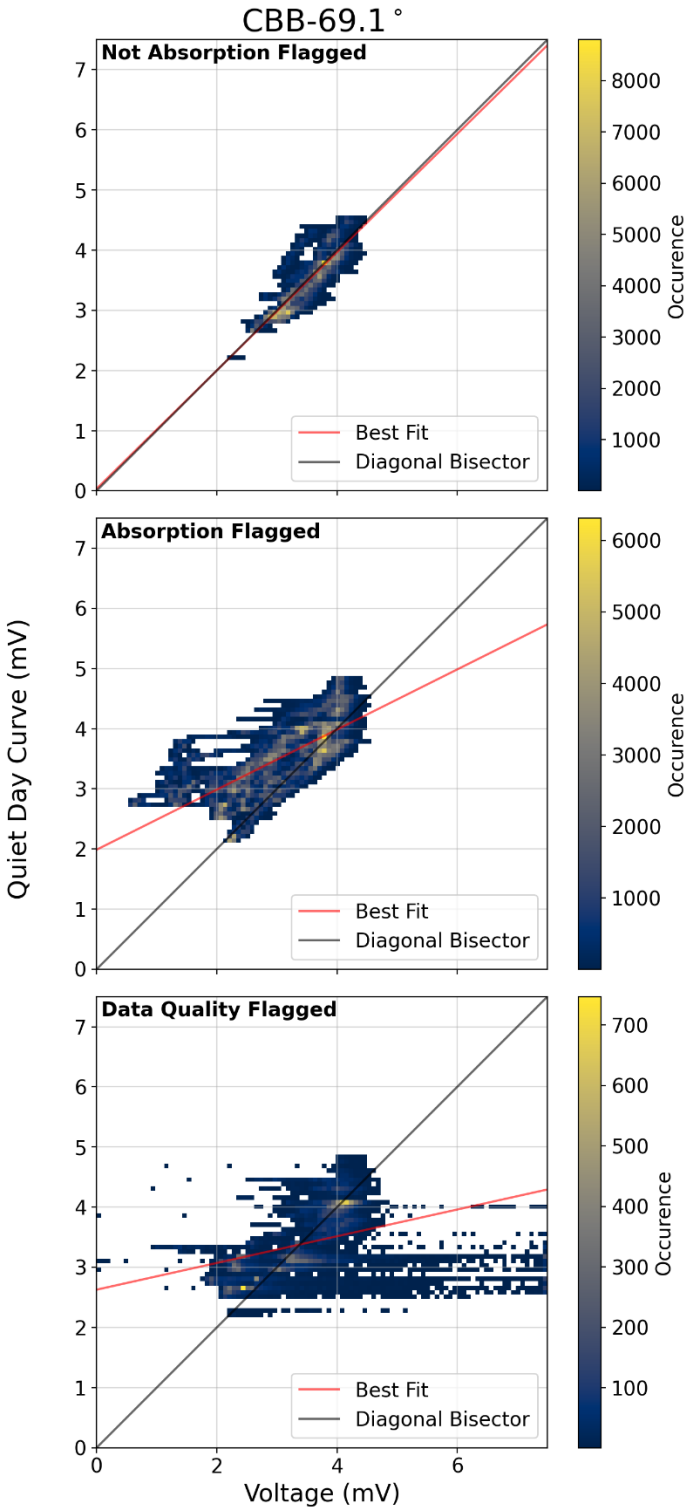

Figure 12: Scatter plots of riometer data from 04-18 September 2017 from Cambridge Bay, NU. Each subplot shows a comparison of measured riometer voltage with calculated QDC values. Top: Periods not determined to have poor data quality, and not associated with absorption ('good'). Middle: Periods automatically determined to be associated with absorption, but otherwise of good quality. Bottom: Periods identified as containing data quality issues. The diagonal bisector, indicating ideal agreement, and the best-fit line to the data are shown in black and red, respectively. Statistics including the slope and intercept of the best-fits, the Pearson correlation coefficient, root mean square error (RMSE), and total number of points are provided in Table 3.

Table 3: Statistical parameters characterizing the relationship between the quiet day curve voltage and voltage measured by the Cambridge Bay riometer, corresponding to Figure 12. Statistics include the slope and intercept of the best-fit line to the data, the Pearson correlation coefficient (ρ), the root mean square error (RMSE), and the number of points displayed in the plot and used to generate the statistics.

	slope	intercept (mV)	ρ	RMSE (mV)	N
Not Absorption Flagged	0.926	0.178	0.748	0.310	568193
Absorption Flagged	0.410	2.24	0.654	0.817	727807
Data Quality Flagged	0.352	2.53	0.469	0.515	177623

Statistics including the slope and intercept of the best-fit lines, the Pearson correlation coefficient, root mean square error (RMSE), and total number of points are provided in Table 3.

When the data are expected to be of good quality and absorption conditions are expected to be quiet, as in the top panel of Figure 12, the agreement between the QDC and measured voltage is strong. The slope of the best-fit line to the data (red) is close to unity (slope = 0.926), closely aligning to the diagonal bisector (black line), the Pearson correlation coefficient (ρ) indicates covariance between the calculated quiet day voltage and measured voltage (ρ=0.748), and the root-mean-square-error (RMSE) is low (RMSE=0.310 mV). When absorption is expected (middle panel), there is a notable grouping of points to the left of the diagonal bisector, indicating the QDC exceeds the measured voltage. Although there are still many points close to the bisecting line, this grouping of points skews the slope of the best-fit line to slope=0.410. Data clusters to the right of the diagonal bisector indicate periods where the QDC is less than the observed voltage, likely representing misfitting of the QDC. While deviations related to misfitting the QDC are not desired, it is expected that more of these would occur in periods, especially extended periods, of expected absorption. This is due the reduction in the number of fitted points contributing to the QDC fit for days with enhanced absorption. The correlation between calculated quiet day voltages and measured voltages is degraded, giving a correlation of ρ=0.654. This is expected as extended absorption events should unevenly reduce measured voltages, reducing the correlation as compared with the periods not flagged for absorption. Additionally, the root-mean-square error (RMSE) associated with absorption periods is significantly larger (0.817 mV) compared with that of quiet periods (0.310 mV). Data flagged as being of poor quality, shown in the lower panel of Figure 12 for the CBB riometer, show degraded correlation (ρ=0.469) and a larger RMSE (0.5155 mV). Data is seen far to the right of the diagonal bisector for these periods, which can also be seen in the top panel of Figure 11 as periods of suddenly elevated voltage readings. The flagging of data quality due to 'spikiness' will asymmetrically be represented in elevated voltage readings during periods of active solar flaring due to radio noise bursts.

Figure 13 shows the 04-18 September 2017 period for the Ottawa, ON (OTT) riometer. Due to its sub-auroral latitude, neither polar cap absorption nor auroral absorption are evident in the calculated absorption. Shortwave fadeout associated with X-class flares on 06, 07, and 10 September 2017 are more evident in calculated absorption for the OTT riometer. As with the data for CBB in Figure 11, some sharp transitions between days can be seen in the QDCs calculated for OTT. This is most evident in the transition from 16 to 17 September (circled in red), due to 'good' flagged periods in the latter portions of 14 September weighing in the fitting parameters, while the earlier absorption flagged portions are not.

In Figure 14, scatter plots show the relationship between measured voltage and calculated QDC for 04-18 September 2017 for quiet periods, possible absorption periods, and likely instrumentation issue periods. The corresponding statistics are provided in Table 4. Similar to Figure 12, the quiet periods (upper panel)

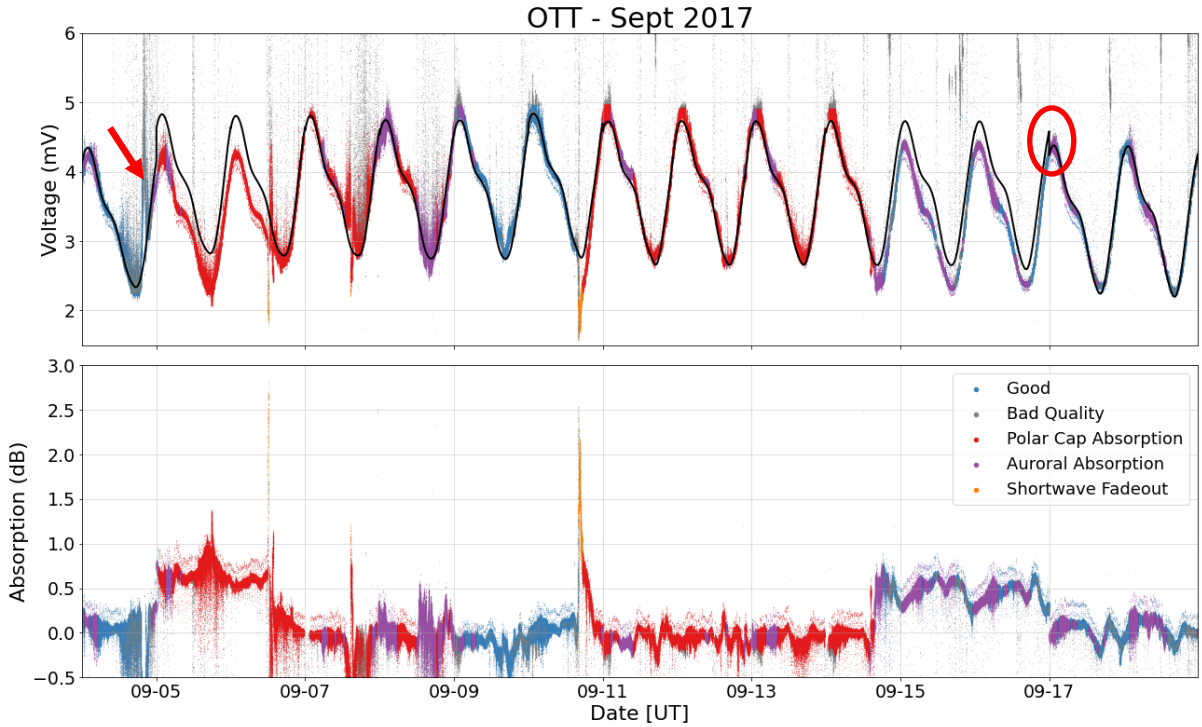

Figure 13: Riometer voltage and absorption for 04-18 September 2017 at Ottawa, ON. Data is color-coded to indicate 'good' (blue) quality data, 'bad' (grey) quality data, polar cap absorption (red), auroral absorption (purple), or shortwave fadeout (orange). A discontinuity in the QDC from 04-05 September has been indicated with a red arrow, and another 16-17 September has been circled in red. Top: Measured voltage and QDC voltage (black line) for the period of interest. Bottom: Calculated absorption for the same period.

show the best agreement between the measured voltage and calculated QDC, with a high density of measurements along the diagonal bisector. The calculated best fit slope of 0.966 is quite close to 1, with a correspondingly high correlation coefficient of ρ=0.952. The RMSE is also less for quiet periods in OTT (0.226 mV), as compared with active periods (0.275 mV; middle panel). The correlation coefficient for active periods is not as low as seen for CBB, with a correlation coefficient of ρ=0.934. The sub-auroral latitude of OTT means that the enhanced absorption seen during polar cap events at CBB is not evident in the OTT data during the absorption flagged periods, resulting in a high correlation coefficient. Data quality flagged periods for OTT (lower panel) show more deviation in the measured voltage from the QDC, with an RMSE of 3.20 mV, and correlation coefficient of ρ=0.163. The slope of the best fit line for these periods (0.0375) is significantly skewed by many saturated high-voltage measurements, identified as radio noise.

Disagreements between the quiet period QDC and measured riometer voltages are attributed to several factors. Changes in the day-to-day QDC are accounted for in the QDC algorithm, but this capacity is reduced during extended periods of heightened absorption, where the algorithm has significantly fewer quiet times to fit to. This is reflected in the time series data as diurnal patterns in calculated absorption, or extended periods of negative absorption. In the scatter plots, misfitting is seen as structuring in the off-diagonal bisector scatter. Other disagreements in the quiet periods are associated with changes in instrument response due to environmental conditions, as described in Section 2. Additionally, changes in radio noise levels can produce increased scatter to the right of the diagonal bisector, as seen in Figure 14. While automated data quality flagging rejects data affected by some of these issues from consideration for quiet periods, they are imperfect tools, and should be supplemented with more comprehensive environmental and instrumentation period removal from quiet periods for research applications.

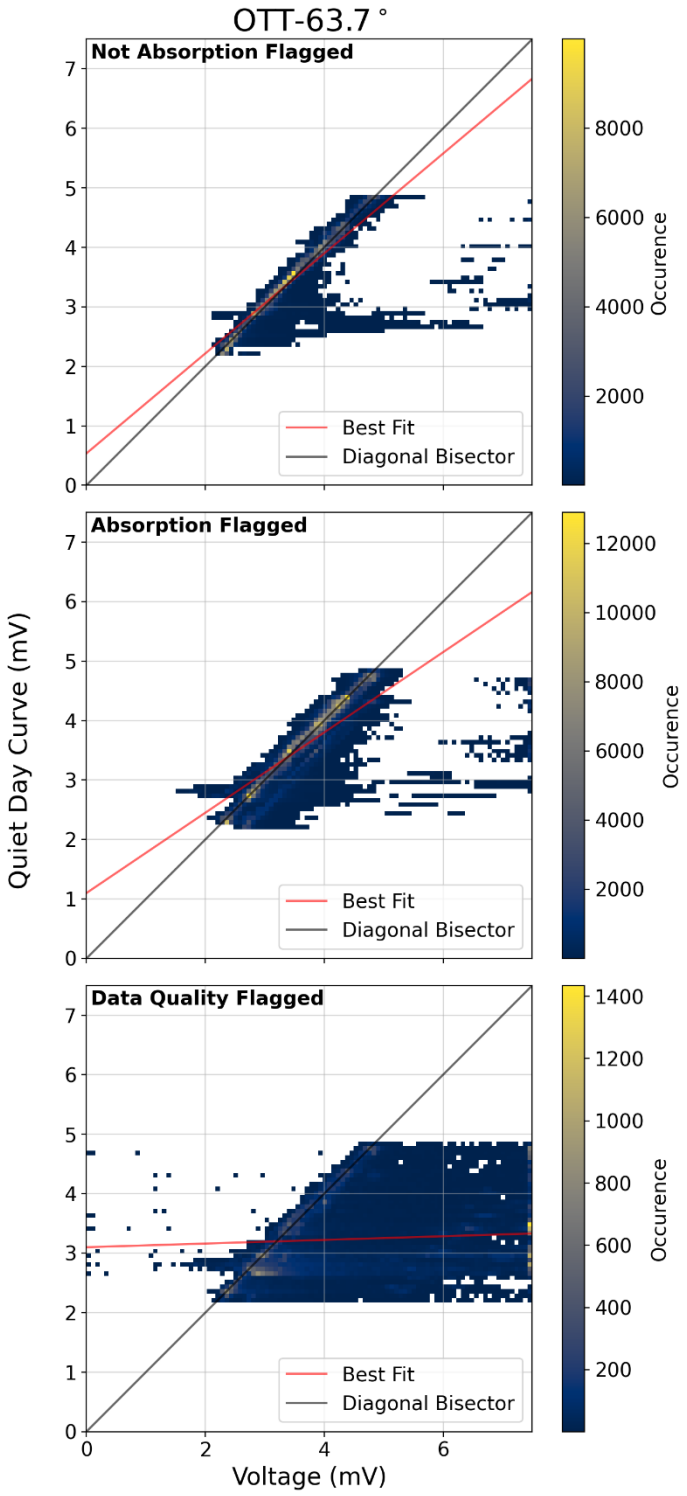

Figure 14: Scatter plots of riometer data from 04-18 September 2017 from Ottawa, ON. Each subplot shows a comparison of measured riometer voltage with calculated QDC values. Top: Periods not determined to have poor data quality, and not associated with absorption ('good'). Middle: Periods automatically determined to be associated with absorption, but otherwise of good quality. Bottom: Periods identified as containing data quality issues. The diagonal bisector, indicating ideal agreement, and the best-fit line to the data are shown in black and red, respectively. Statistics including the slope and intercept of the best-fits, the Pearson correlation coefficient, root mean square error (RMSE), and total number of points are provided in Table 4.

Table 4: Statistical parameters characterizing the relationship between the quiet day curve voltage and voltage measured by the Ottawa riometer, corresponding to Figure 14. Statistics include the slope and intercept of the best-fit line to the data, the Pearson correlation coefficient (ρ), the root mean square error (RMSE), and the number of points displayed in the plot and used to generate the statistics.

	slope	intercept (mV)	ρ	RMSE (mV)	N
Not Absorption Flagged	0.966	0.192	0.952	0.226	528023
Absorption Flagged	0.903	0.473	0.934	0.275	767977
Data Quality Flagged	0.0375	3.330	0.163	3.20	122721

During periods where absorption is expected, as seen in Figure 12 and Figure 14, the scatter plots nevertheless include a number of points lying along the diagonal bisector. Agreement during these periods indicate absorption is being over-identified. This is much more evident in the OTT data in Figure 14, due to the nature of the auroral absorption and polar cap absorption flagging algorithms, which do not incorporate latitude information. This results in increased over-flagging for sub-auroral riometers. Although this process ensures that only quiet data are included when determining the QDC, care should be taken in using the absorption flags for research purposes.

The nature of noise or instrumentation issues associated with 'bad' quality periods will naturally produce some structure in their relation to the quiet day curve. 'Spiky' data related to probable radio noise, such as seen in the top panel of Figure 13 for the OTT riometer, produces an asymmetric spread of data to the right of the diagonal bisector, as previously mentioned, and seen most prominently in the bottom panel of Figure 14. It is important to note is that there are numerous points along the diagonal bisector for quality flagged periods, evident in both the CBB and OTT riometers, indicating over-flagging of these periods. Further refinement of data quality flags through additional use of supplementary data sources (for identification of radio noise, weather-driven instrument variability, etc.), and operator intervention would improve data quality flagging accuracy. Data flagged as being of poor quality constitutes about ~12% of the CBB data set, and 8.6% of the OTT data set for this event. A significant portion of the data flagged as poor in the CBB data set arises from flagging of solar radio noise – the over identification of this for CBB degrades the quality of agreement for this riometer. Over identification of solar radio noise can be seen in Figure 11 as erroneous bad data flags in the peaks of the QDCs. A more precise metric for removing solar radio noise from riometer data may be a desirable direction for future work. Overly generous quality flagging is useful for operational use, to better fit the QDC for characterizing absorption, but its presence should be noted for other applications. The evidence of over flagging of the data does stress the need for post-processing and observer intervention for its use in research.

The agreement between the calculated QDC with measured riometer voltages for quiet periods of good data quality, and the degradation of the agreement for periods flagged as likely containing absorption, is an indicator that the automated QDC algorithm is functioning well in an operational capacity. This methodology will not always accurately fit quiet day variations in measured riometer voltages; generally, effects produced by terrestrial weather, or intermittent instrumentation effects will not be represented well by this methodology. Extended periods of persistent enhanced absorption may also result in some systematic misfitting of the QDC. Additionally, over-flagging of absorption can result in the mislabeling of quiet periods. Nevertheless, the ability of the algorithm to determine absorption in near-real time is a useful tool for measuring space weather impacts on radio propagation in the ionosphere in an operational capacity.

7. Near real-time implementation

This algorithm has been implemented for near-real time calculation of ionospheric absorption in the NRCan riometer network. During a solar proton event with concurrent polar cap absorption occurring 08-11 May 2023, the near-real time riometer data processing algorithm described here was in operation. Riometer data were processed every 15 minutes, QDCs were evaluated at the start of each day, and riometer data was plotted in near-real time. Figure 15 and Figure 16 show the live-plotting results for 07-09 May 2023, sampled at 01:56 UT 09 May 2023. Voltage is plotted in Figure 15 and absorption is plotted in Figure 16 in panels corresponding to selected NRCan riometer stations, where green and pink line colouring indicates good and bad data quality periods, respectively. The QDC is overplotted in each panel of Figure 15 in black. Riometer stations (see Table 1) are represented in order of decreasing geographic latitude from RES (74.7°N) to OTT (45.4°N). Periods where auroral absorption and polar cap absorption were flagged according to Section 4, and are indicated by green and purple shading. Grey shading indicates when the riometer station is on the nightside according to the local SZA. Prior to the onset of auroral and polar cap absorption, the riometer-derived absorption, is near zero, except for a few stations, as discussed below. Absorption begins to enhance for stations poleward of YKC between 0 and 12 UT on 08 May 2011 prior to the >10 MeV solar proton flux crossing the 10 pfu threshold, represented by the green shading. During this period absorption is <1 dB. As the event progresses and the 10 pfu threshold is crossed absorption becomes elevated above 1 dB at RES, CBB, and YKC, and minor enhancements are observed at BRD. Interspersed within the period of expected polar cap absorption are four auroral absorption periods coinciding with elevated auroral zone geomagnetic activity. The third period of auroral absorption coincides with enhanced absorption observed by the YKC riometer, located on the nightside at this time.

Also of note are instances of poor data quality which affect the QDC algorithm's ability to appropriately fit a QDC and calculate absorption. Some riometers, such as IQA, YKC, and particularly MEA, show high levels of variation. This results in a reduced confidence in the ability to accurately calculate absorption for the riometers, though the algorithm still does produce a QDC with some ability to track the quiet variations of these riometers. Overall, the algorithm performed well in provide a near-real time absorption data product for space weather duty forecasters.

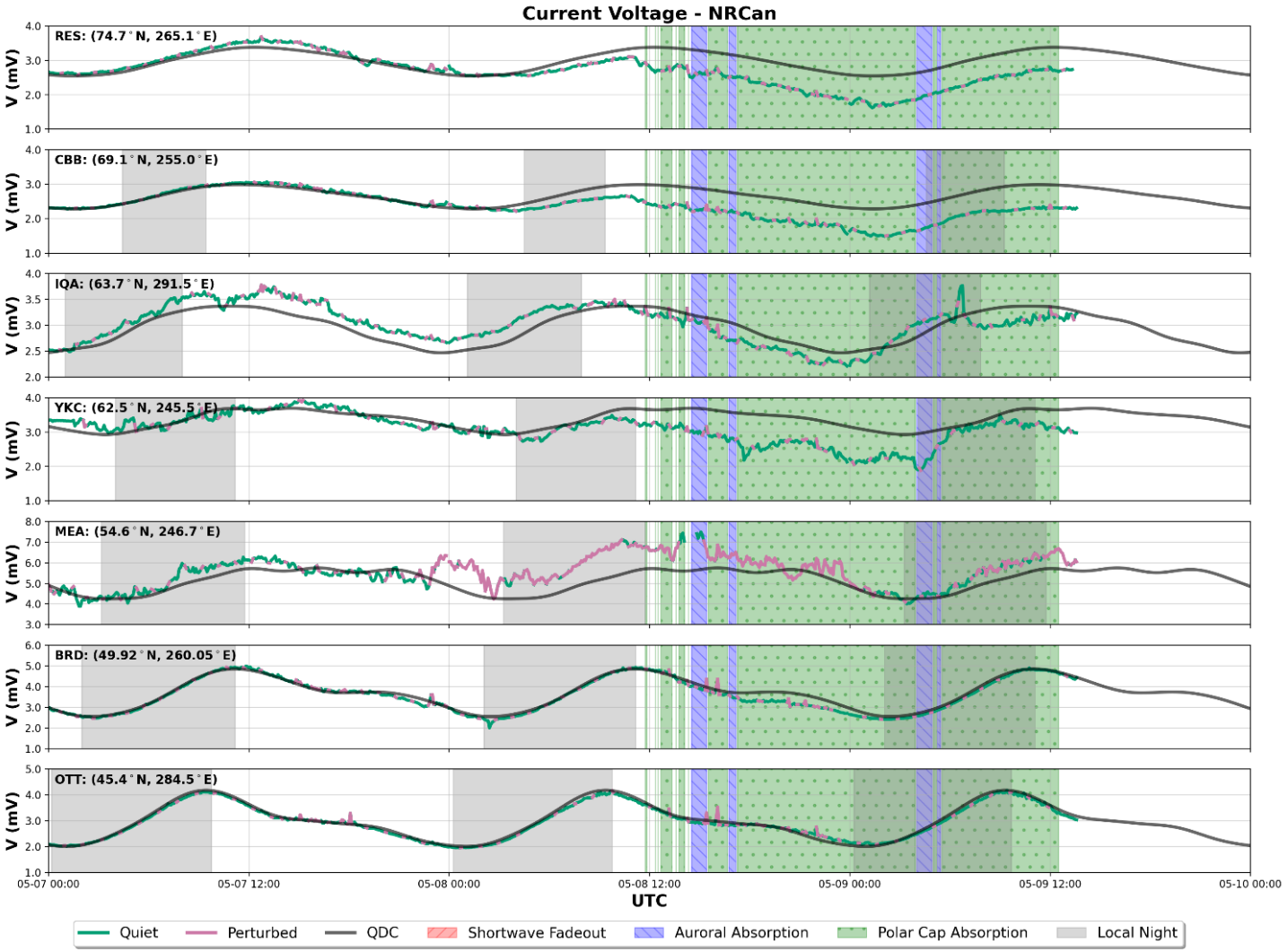

PCA is flagged from GOES >10 MeV proton flux, AA is flagged using CANMOS auroral zone magnetometers, and SWF is flagged using GOES 0.1-0.8 nm X-ray flux and Solar Zenith Angle.

Figure 15: Near-real time plots of riometer voltages for selected NRCan riometer stations on 09 May 2023. Color shaded regions denote times designated for likely absorption. These data were taken during a solar proton event, as indicated from the green shaded polar cap absorption periods.

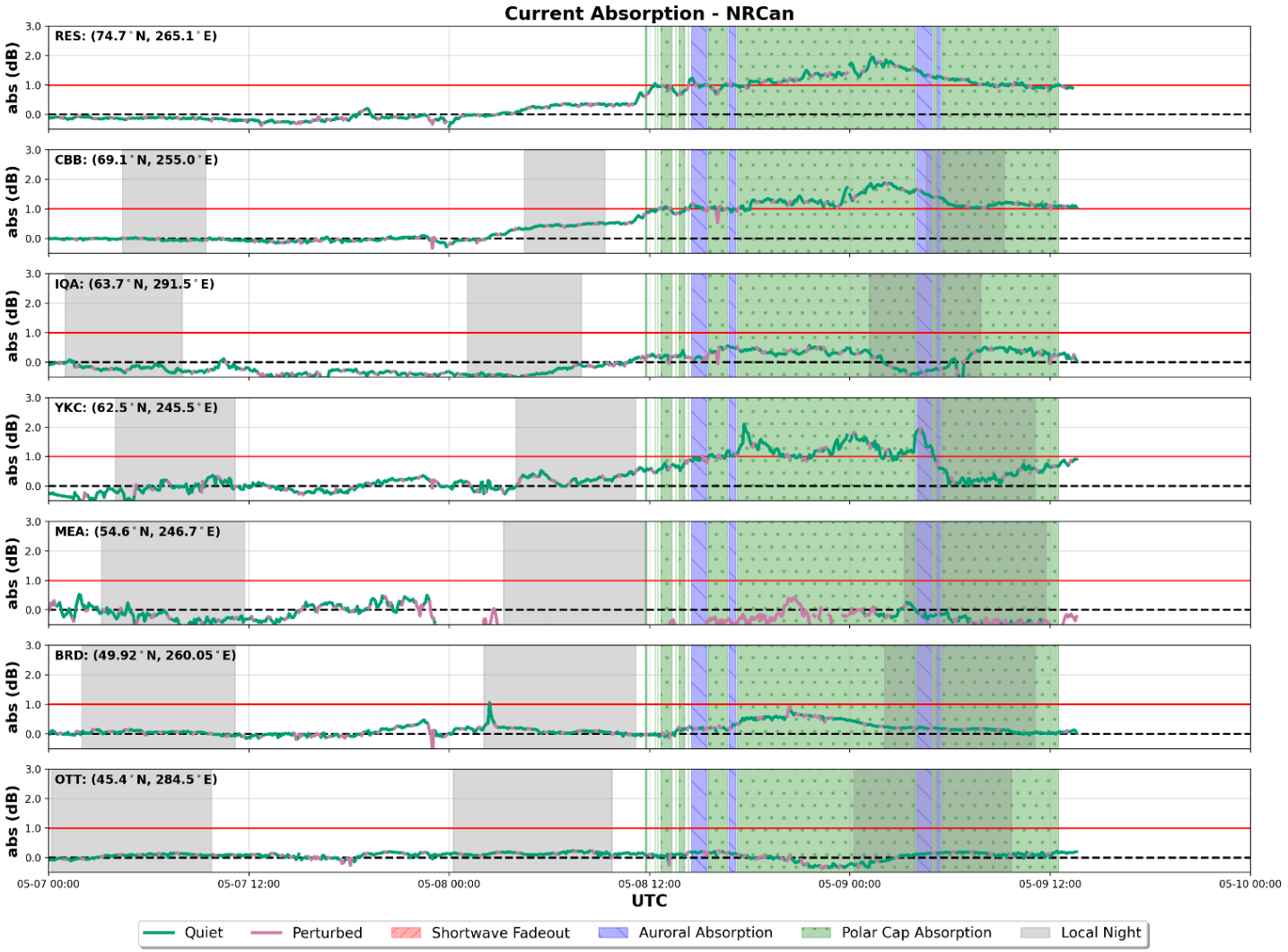

Figure 16: Near-real time plots of riometer absorptions for selected NRCan riometer stations on 09 May 2023. Color shaded regions denote times designated for likely absorption. These data were taken during a solar proton event, as indicated from the green shaded polar cap absorption periods. The 1dB absorption threshold is indicated to assist duty forecasters to assess ionospheric conditions.

8. Summary

This report describes the algorithm developed by the Canadian Hazards Information Service for processing riometer data in near-real time. Data are passed through a filter to remove data collected during calibration periods, and data that are corrupt or missing. Next, data are put through despiking and solar radio noise flagging algorithms. Periods where the stations are likely to observe absorption are next identified. Shortwave fadeout is determined based on the magnitude of the 0.1-0.8 nm solar X-ray flux and the solar zenith angle of the observing station. Auroral absorption is flagged based on a proxy AE index derived from local geomagnetic perturbations, and polar cap absorption is evaluated based on a threshold of 10 pfu in the >10 MeV solar proton flux.

Proper identification of periods where absorption is likely to be observed is important in fitting a quiet day curve to the data. As the title indicates, a quiet day curve represents 'quiet' periods and must be fit to data free of absorption. Although short-term effects like shortwave fadeout are not likely to impact quiet day curve determination, a prolonged multi-hour auroral absorption or multi-day polar cap absorption event will. The consequence is a quiet day curve that underestimates the deviation of the observed voltage from the background level, and therefore underestimates absorption. Accurate absorption is necessary to constrain absorption models for near-real time operational use, or for accurate representation of the data for visual displays used to evaluate, for example, the ionospheric impact of space weather events. The inclusion of two weeks of riometer data for calculation of the quiet day curve is intended to allow for calculation of the quiet day curve, even during periods of ionospheric absorption. Consideration of ionospheric absorption and data quality flags allow for reasonably accurate quiet day curves, suitable for use as an operation data product.

The near-real time filtering of riometer data and automated quiet day curve generation described in this report provide a reliable automated data processing algorithm for a conservative determination of absorption appropriate for operational use. To use the data to further our understanding of the underlying physical processes, additional filtering ensuring all potential contamination sources are removed is recommended.

9. References

Agy, V. (1970), HF radar and auroral absorption, Radio Science, 5(11), pp. 1317-1324, https://doi.org/10.1029/RS005i011p01317.

Baker, D. N., P. Stauning, E. W. Hones Jr., P. R. Higbie, and R. D. Belian (1981), Near-equatorial, high-resolution measurements of electron precipitation at L≈6.6, J. Geophys. Res., 86(A4), pp. 2295-2313, https://doi.org/10.1029/JA086iA04p02295.

Basler, R. P. (1963), Radio wave absorption in the auroral ionosphere, J. Geopys. Res., 68 (16), pp. 4665-4681, https://doi.org/10.1029/JZ068i016p04665.

Browne, S., J. K. Hargreaves, and F. Honary (1995). An imaging riometer for ionospheric studies, Electronics & Communication Engineering Journal, 7(5), 209-217, https://doi.org/10.1049/ecej:19950505.

Cannon, P., M. Angling, L. Barclay, C. Curry, C. Dyer, R. Edwards, G. Greene, M. Hapgood, R. Horne, D. Jackson, C. Mitchell, J. Owen, A. Richards, C. Rogers, K. Ryden, S. Saunders, M. Sweeting, R. Tanner, A. Thomson, and C Underwood (2013), Extreme space weather: impacts on engineered systems and infrastructure. London, Royal Academy of Engineering

Chisham, G., et al. (2007), A decade of the Super Dual Auroral Radar Network (SuperDARN): scientific achievements, new techniques and future directions, Surveys in Geophysics, 28 (1), 33–109, https://doi.org/10.1007/s10712-007-9017-8.

Chivers, H. (1974), Solid State Riometer Manua, La Jolla Sciences, USA, (Reprint October 1980)

Coyne., V. J. (Ed.)(1979), Special topics in HF propagation, AGARD Conf. Proc. No. 263, Advisory Group for Aerospace Research and Development, North Atlantic Treaty Organization.

Danskin, D. W., D. Boteler, E. Donovan, and E. Spanswick (2008), The Canadian riometer array, Proc. of the 12th International Ionospheric Effects Symposium, IES 2008

Davies, K. (1990), Ionospheric Radio, IEE Electromagn, Ser. Peter Peregrinus, London, vol. 31.

Davis, T. N., and M. Sugiura (1966), Auroral electrojet activity index AE and its universal time variations, J. Geophys. Res., 71 (3), pp. 785-801, https://doi.org/10.1029/JZ071i003p00785.

Driatsky, V. M. (1966), Study of the space and time distribution of auroral absorption according to observations of the riometer network in the Arctic, Geomagnetism and Aeronomy, 6, pp. 828.

Fiori, R. A. D, L. Trichtchenko, C. Balch, E. Spanswick, and S. Groleau (2020). Characterizing auroral-zone absorption based on global Kp and regional geomagnetic hourly range indices, Space Weather, 18(12), https://doi.org/10.1029/2020SW002572.

Fiori, R. A. D., S. Chakraborty, and L. Nikitina (2022a). Data-based optimization of a simple shortwave fadeout absorption model, Journal of Atmospheric and Solar-Terrestrial Physics, 230, https://doi.org/10.1016/j.jastp.2022.105843.

Fiori, R. A.D, V. V. Kumar, D. H. Boteler, and M. B. Terkildsen. (2022b). Occurrence rate and duration of space weather impacts to high frequency radio communication used by aviation, Journal of Space Weather and Space Climate, 12(21), https://doi.org/10.1051/swsc/2022017.

Foppiano, A. J., and P. A. Bradley (1983), Prediction of auroral absorption of high-frequency waves at oblique incidence, Telecommunication Journal, 50(10), pp. 547-560.

Foppiano, A. J., and P. A. Bradley (1984), Day-to-day variability of riometer absorption, J. Atmos. Terr. Phys., 46 (8), pp. 689-696, https://doi.org/10.1016/0021-9169(84)90130-2.

Hargreaves, J. K. (1966), On the variation of auroral radio absorption with geomagnetic activity, Planet. Space Sci., 14, pp. 991-1006.

Hargreaves, J. K. (1969), Auroral absorption of HF radio waves in the ionosphere: A review of results from the first decade of riometry, Proceedings of the IEEE, 57(8).

Hargreaves, J. K. (2007), Seasonal variations in the incidence of auroral radio absorption events at very high latitude, and the influence of the magnetotail, Ann. Geophys., 25, pp. 711-720, https://doi.org/10.5194/angeo-25-711-2007.

Hargreaves, JK. 2010. Auroral radio absorption: The prediction question. Adv. Space Res., **45.** https://doi.org/10.1016/j.asr.2009.10.026.

Hargreaves, J. K., and F. C. Cowley (1967), Studies of auroral radio absorption events at there magnetic latitudes – I occurrence and statistical properties of the events, Planet. Space Sci, 15, pp. 1571-1583, https://doi.org/10.1016/0032-0633(67)90090-6.

Hargreaves, J. K., H. Ranta, A. Ranta, E. Turunen, and T. Turunen (1987), Observations of the polar cap absorption event of February 1984 by the Eiscat incoherent scatter radar, Planet. Space Sci., 35 (7), pp. 947-958, https://doi.org/10.1016/0032-0633(87)90072-9.

Hartz, T. R., L. E. Montbriand, and E. L. Vogan (1963), A study of auroral absorption at 30 MC/S, Canadian Journal of Physics, 41, pp. 581-595.

Holt, C., B. Landmark, and F. Lied (1961) Analysis of riometer observations obtained during polar radio blackouts, J. Atmos. and Terr. Phys., 23, pp. 229-230, https://doi.org/10.1016/0021-9169(61)90048-4.

Hruska, J., and R. L. Coles (1987), A new type of magnetic activity forecast for high geomagnetic latitudes, Journ. of Geomag. and Geoelectr., 39(9), 521-534, https://doi.org/10.5636/jgg.39.521.

Hunsucker, R. D., and J. K. Hargreaves (2003). The high-latitude ionosphere and its effects on radio propagation. Cambridge atmospheric and space science series, Cambridge University Press, Cambridge.

ICAO (2018), Annex 3 to the Convention on International Civil Aviation, Meteorological Service for International Air Navigation, ICAO International Standards and Recommended Practices, Twentieth Edition, July 2018, http://store.icao.int/products/annex-3-meteorological-service-for-international-air-navigation (last accessed 11 June 2020).

ICAO (2019), Manual on Space Weather Information in Support of International Air Navigation, ICAO Doc 10100, First Edition, https://store.icao.int/products/manual-on-space-weather-information-in-support-of-international-air-navigation-doc-10100 (last accessed 11 June 2020).

Kavanagh, A. J., S. R. Marple, F. Honary, I. W. McCrea, A. Senior (2004a). On solar protons and polar cap absorption: constraints on an empirical model. Ann. Geophys., **22:**3. https://doi.org/10.5194/angeo-22-1133-2004.

Kavanagh A.J., M. J. Kosch, F. Honary, A. Senior, S. R. Marple, E. E. Woodfield, and I. W. McCrea I.W (2004b). The statistical dependence of auroral absorption on geomagnetic and solar wind parameters, Ann. Geophys., volume 22, issue3, pp. 877-887, https://doi.org/10.5194/angeo-22-877-2004.

Kellerman, A. C., and R. A. Makarevich (2011), The response of auroral absorption to substorm onset: Superposed epoch and propagation analyses, J. Geophys. Res., 116(A05312), https://doi.org/10.1029/2010JA015972.

Knipp, D. J., V. Bernstein, K. Wahl, H. Hayakawa (2021). Timelines as a tool for learning about space weather storms. J. Space Weather Space Clim., 11(29). https://doi.org/10.1051/swsc/2021011.

Lam, H.-L. (2011), From early exploration to space weather forecasts: Canada's geomagnetic odyssey. Space Weather, 9, https://doi.org/10.1029/2011SW000664.

Levine, E. V., P. J. Sultan, L. I. Teig (2019). A parameterized model of X-ray solar flare effects on the lower ionosphere and HF propagation. Radio Science, 54, https://doi.org/10.1029/2018RS006666.

Little, C. G., & Leinback, H. (1959). The riometer – a device for the continuous measurement of ionospheric absorption. *Proceedings of the IRE.* 315-320.

Menvielle, M., and A. Berthelier (1991), The K-derived planetary indices: description and availability, Reviews of Geophysics, 29 (3), pp. 415-432, https://doi.org/10.1029/91RG00994.

Mitra, A. 1974. Ionospheric effects of solar flare, vol. 46, Astrophysics and space science library. Massachusetts: Reading. https://doi.org/10.1007/978-94-010-2231-6.

National Research Council (2008), Severe space weather events – Understanding societal and economic impacts: a workshop report, Natl. Acad. Press, Washington, D.C., pp 144.

Neal, J. J., C. J. Rodger, and J. C. Green (2013). Empirical determination of solar proton access to the atmosphere: Impact on polar flight paths, Space Weather, 11, 420-4333, https://doi.org/10.1002/swe.20066.

Newell, P. T., R. A. Greenwald, and J. M. Ruohoniemi (2001), The role of the ionosphere in aurora and space weather, Reviews of Geophysics, 39(2), pp. 137-149, https://doi.org/10.1029/1999RG000077.

NORSTAR (2014). CANOPUS quiet day curve generation. Available online: http://aurora.phys.ucalgary.ca/norstar/rio/doc/CANOPUS_Riometer_Baselining.pdf (accessed 01 March 2019).

Pirjola, R., K. Kauristie, H. Lappalainen, A. Viljanen, and A. Pulkkinen (2005), Space weather risk, Space Weather, 3 (S02A02), https://doi.org/10.1029/2004SW000112.

Rodger, C. J., A. J. Kavanagh, M. A. Clilverd, and S. R. Marple (2013), Comparison between POES energetic electron precipitation observations and riometer absorptions: Implications for determining true precipitation fluxes. J. Geophys. Res., 118(12), pp. 7810-7821, https://doi.org/10.1002/2013JA019439.

Rogers, N. C., and F. Honary (2015), Assimilation of real-time riometer measurements into models of 30 MHz polar cap absorption, Journal of Space Weather and Space Climate, 5, pp. 1-18., https://doi.org/10.1051/swsc/2015009.

Rogers, N. C., A. Kero, F. Honary, P. T. Verronen, and E. M. Warrington (2016), Improving the twilight model for polar cap absorption nowcasts, Space Weather, 14, 950-972, https://doi.org/10.1002/2016SW001527.

Sauer, H., and D. C. Wilkinson (2008), Global mapping of ionospheric HF/VHF radio wave absorption due to solar energetic protons, Space Weather, 6, S12002, https://doi.org/10.1029/2008SW000399.

Sigernes, F., M. Dyrland, P. Brekke, S. Chernouss, D. A. Lorentzen, K. Oksavik, and C. S. Deehr (2011), Two methods to forecast auroral displays, J. Space Weather Space Clim, 1 (A03), https://doi.org/10.1051/swsc/2011003.

Thayaparan, T., Y. Ibrahim, J. Polak, and R. Riddolls (2018), High-frequency over-the-horizon-radar in Canada, IEEE Trans. Geosci. Remote Sens., 15(11), pp. 1700-1704, https://doi.org/10.1109/LGRS.2018.2856185.

Turunen, E., H. Matveinen, J. Tolvanen and H. Ranta (1996). D-region ion chemistry model. .), Solar-Terrestrial Energy Program: Handbook of Ionospheric Models, SCOSTEP Secretariat, Boulder, Colorado, pp. 1-26.

Yamazaki, Y., J. Matzka, C. Stolle, G. Kervalishvili, J. Rauberg, O. Bronkalla, A. Morschauser, S. Bruinsma, Y.Y. Shprits, D.R. Jackson (2022). Geomagnetic Activity Index Hpo. Geophysical Research Letters, 49(10), https://doi.org/10.1029/2022GL098860.

Zawdie, K. A., D. P. Drob, D. E. Sisking, and C. Coker (2017), Calculating the absorption of HF radio waves in the ionosphere, Radio Science, 52, pp. 767-783, https://doi.org/10.1002/2017RS006256.